Beyond the angle of repose: A review and synthesis of landslide processes in response to rapid uplift, Eel River, Northern California

Joshua J. Roering[1], Benjamin H. Mackey[2], Alexander L. Handwerger[1], Adam M. Booth[3], David A. Schmidt[4], Georgina L. Bennett[1], and Corina Cerovski-Darriau[1]

[1] Department of Geological Sciences
University of Oregon
Eugene, OR 97403-1272
USA

[2] Department of Geological Sciences
University of Canterbury
Private Bag 4800
Christchurch 8140
New Zealand

[3] Department of Geology
Portland State University
PO Box 751
Portland, OR 97207-0751
USA

[4] Department of Earth and Space Sciences
University of Washington
4000 15th Avenue NE
Seattle, WA 98195-1310
USA

corresponding author:
jroering@uoregon.edu
541 346 5574

Abstract

In mountainous settings, increases in rock uplift are often followed by a commensurate uptick in denudation as rivers incise and steepen hillslopes, making them increasingly prone to landsliding as slope angles approach a limiting value. For decades, the threshold slope model has been invoked to account for landslide-driven increases in sediment flux that limit topographic relief, but the manner by which slope failures organize themselves spatially and temporally in order for erosion to keep pace with rock uplift has not been well documented. Here, we review past work and present new findings from remote sensing, cosmogenic

1

radionuclides, suspended sediment records, and airborne lidar data, to decipher patterns of landslide activity and geomorphic processes related to rapid uplift along the northward-migrating Mendocino Triple Junction in Northern California. From historical air photos and airborne lidar, we estimated the velocity and sediment flux associated with active, slow-moving landslides (or earthflows) in the mélange- and argillite-dominated Eel River watershed using the downslope displacement of surface markers such as trees and shrubs. Although active landslides that directly convey sediment into the channel network account for only 7% of the landscape surface, their sediment flux amounts to more than 50% of the suspended load recorded at downstream sediment gauging stations. These active slides tend to exhibit seasonal variations in velocity as satellite-based interferometry has demonstrated that rapid acceleration commences within 1 to 2 months of the onset of autumn rainfall events before slower deceleration ensues in the spring and summer months. Curiously, this seasonal velocity pattern does not appear to vary with landslide size, suggesting that complex hydrologic-mechanical feedbacks (rather than 1-D pore pressure diffusion) may govern slide dynamics. A new analysis of 14 years of discharge and sediment concentration data for the Eel River indicates that the characteristic mid-winter timing of earthflow acceleration corresponds with increased suspended concentration values, suggesting that the seasonal onset of landslide motion each year may be reflected in the export of sediments to the continental margin. The vast majority of active slides exhibit gullied surfaces and the gully networks, which are also seasonally active, may facilitate sediment export although the proportion of material produced by this pathway is poorly known.

Along Kekawaka Creek, a prominent tributary to the Eel River, new analyses of catchment-averaged erosion rates derived from cosmogenic radionuclides reveal rapid erosion (0.76 mm/yr) below a prominent knickpoint and slower erosion (0.29 mm/yr) upstream. Such knickpoints are frequently observed in Eel tributaries and are usually comprised of massive (>10 m) interlocking resistant boulders that likely persist in the landscape for long time periods (>10^5 yr). Upstream of these knickpoints, active landslides tend to be less frequent and average slope angles are slightly gentler than in downstream areas, which indicates that landslide density and average slope angle appear to increase with erosion rate. Lastly, we synthesize evidence for the role of large, catastrophic landslides in regulating sediment flux and landscape form. The emergence of resistant blocks within the mélange bedrock has promoted large catastrophic slides that have dammed the Eel River and perhaps generated outburst events in the past. The frequency and impact of these landslide dams likely depend on the spatial and size distributions of resistant blocks relative to the width and drainage area of adjacent valley networks. Overall,

our findings demonstrate that landslides within the Eel River catchment do not occur randomly, but instead exhibit spatial and temporal patterns related to baselevel lowering, climate forcing, and lithologic variations. Combined with recent landscape evolution models that incorporate landslides, these results provide predictive capability for estimating erosion rates and managing hazards in mountainous regions.

Key words: Landslide; Lidar; Landscape evolution; Insar; Erosion; Suspended sediment

1. Introduction

In mountainous landscapes, landslides liberate soil and bedrock in response to tectonic uplift (e.g., Brunsden, 1999; Roering et al., 2005; Korup et al., 2007, 2010; Agliardi et al., 2013; Ekstrom and Stark, 2013). Characterizing how landslides contribute to landscape evolution in mountainous regions is challenging given that diverse geologic, climatic, and even biological factors influence slope stability. For example, relatively subtle variations in rock properties can dictate whether a mountain range will be subject to infrequent, deep-seated bedrock slumps or frequent rockfall and shallow landslides (e.g., Korup, 2008). Similarly, runout dynamics and material properties determine whether landslide materials deposited in valleys will tend to resist breaching and form lakes or become subject to downstream dispersal soon after failure occurs (e.g., Costa and Schuster, 1988; Iverson et al., 2000). These highly disparate responses highlight the challenge and importance of characterizing landslide processes in order to interpret and predict their role in shaing landscapes (Cendrero and Dramis, 1999). In this contribution, we review past work and highlight several new analyses that describe landslide dynamics and related geomorphic processes in response to rapid uplift in the Northern California Coastal Ranges. The approaches described here span a range of spatial and temporal scales, emphasizing the importance of integrating diverse tools for assessing how landslides shape mountainous terrain.

Early efforts to conceptualize landslide behavior over geologic timescales used the analogy of a dry sandpile to represent how landslides influence hillslope form and sediment fluxes (de la Noe and de Margerie, 1888; Strahler, 1950; Carson and Petley, 1970; Bak et al., 1987, 1988; Burbank et al., 1996; Densmore et al., 1997; Montgomery, 2001). In the sandpile analogy, when channels incise at a sufficient pace, hillslopes attain a threshold slope or 'angle of repose' as sand avalanches displace material downslope and generate erosion at a rate equal to that of river incision (Roering, 2012). Increasing the rate of incision has the effect of increasing the rate

at which hillslopes deliver sand avalanches to channels but does not increase hillslope steepness because the maximum stable angle cannot be exceeded. This simple conceptual model implies that channel incision is immediately followed by uniform hillslope lowering of the same magnitude. In other words, the threshold slope model, strictly interpreted, suggests that hillslope erosion is directly and instantaneously coupled to vertical lowering of the valley network and occurs as uniform 'sheets' of erosion. While this framework is intuitively appealing, landslide erosion on natural hillslopes, and even laboratory sandpiles, does not manifest as contiguous sheets of cascading sediment or bedrock (Densmore et al, 1997; Roering et al., 2001; Malamud et al., 2004). Instead, both natural and experimental slopes exhibit discrete slope failures that are highly variable in both space and time. Many of the local factors that influence the propensity for landsliding are highly stochastic and difficult to characterize (e.g., rock mass strength, pore pressures, vegetation, rock fabric and slope orientation, the intensity and extent of storms, earthquake magnitude and recurrence, and channel–hillslope interactions) (Brunsden, 1993). As a result, it has proven challenging to test the central tenet of the threshold slope model: do natural hillslopes achieve a threshold state such that landslide erosion balances channel incision? Furthermore, assuming that slide-driven erosion can pace channel lowering, how do landslides organize themselves spatially and temporally in order to maintain this balance? Capturing and quantifying the relevant landslide patterns to tackle these queries proved beyond our reach until the accumulation of high-resolution remote sensing imagery in recent decades.

Landslide inventories are often produced by documenting failures over a given time interval or following major storms, earthquakes, or snowmelt events, and have become a favored tool for addressing how landslides influence landscape evolution (e.g., Hovius et al., 1997; Malamud et al., 2004; Schwab et al., 2008; Harp et al., 2011; Bennett et al., 2012; Larsen and Montgomery, 2012). These inventory studies are sometimes accomplished through field mapping but more typically via air photos, satellite imagery, or airborne lidar (Nichol and Wong, 2005; Guzzetti et al., 2012; Borgomeo et al., 2014; Tarolli, 2014). These studies often reveal that landslide density decreases nonlinearly with landslide area and in some cases the slope of this relationship implies that infrequent large landslides exhibit a disproportionate influence on denudation and valley dynamics (Stark and Hovius, 2001; Korup et al., 2007, Agliardi et al., 2013; Giordan et al., 2013). Numerous studies have proposed functional relationships to describe landslide area distributions, including commonly observed decreases (or rollovers) in frequency at small landslide areas that reflect changing landslide mechanics (Katz and

Aharonov, 2006; Brunetti et al., 2009; Stark and Guzzetti, 2009), detection limitations due to data resolution (Simoni et al., 2013), or heterogeneity in boundary conditions (Pelletier et al., 1997; Roering et al., 2005).

When coupled with chronological constraints as well as depth-area scaling data, landslide density functions can be used to calculate denudation rates and determine the extent to which landslide erosion balances rock uplift (Hovius et al., 1997; Malamud et al., 2004; Larsen and Montgomery, 2012). Initial efforts to integrate slide-driven fluxes indicate that denudation rates are of the same order as independently derived proxies for rock uplift (Hovius et al., 1997; Clarke and Burbank, 2010; Larsen and Montgomery, 2012). The findings of Larsen and Montgomery (2012) suggest that increases in exhumation (and presumably incision) tend to increase the frequency of all landslide sizes rather than exclusively influence the relative importance of large failures. That said, landslide erosion rate estimates are subject to significant uncertainty associated with noisy scaling relationships (Guzzetti et al., 2012; Korup et al., 2012; Larsen and Montgomery, 2012; Simoni et al., 2013), subjective and uncertain landslide mapping (van den Eeckhaut et al., 2007; DeLong et al., 2012), and short time intervals. Nonetheless, these endeavors have profoundly advanced our understanding of the landslide contribution to erosion.

In steep, bedrock-dominated landscapes, landslides tend to evacuate their initiation sites upon failure such that slide material translates wholly into valleys, facilitating rather straightforward mapping, with some exceptions (Parker et al., 2011; Li et al., 2014). Landscape evolution models for these settings surmise that once a landslide occurs, failure does not tend to recur at that location until rock properties and hillslope geometry have evolved sufficiently to promote failure in the future (Densmore et al., 1997, Egholm et al., 2013). In these settings, bedrock properties, seismicity, climatic variables, topographic variations, and position within the valley network are among the many factors that can contribute to highly stochastic landslide patterns (Palmquist and Bible, 1980). As a result, it can be difficult to decipher the role of topography and climate, for example, in modulating how landslides are distributed temporally and spatially in order to keep pace with rock uplift and incision. Apart from studies of earthquake-triggered landsliding (Keefer, 1994, 2002; Densmore and Hovius, 2000; Meunier et al., 2008; Huang et al., 2012), few inventories have addressed how landslides are spatially distributed in relation to topography and other geologic forcings (Scheingross et al., 2013).

Less imposing (i.e., gentle and accessible) geologic settings, specifically those that promote earthflow erosion, provide an alternative venue for evaluating short- and long- timescale landslide dynamics in response to rapid rock uplift and baselevel lowering. Earthflow-style landslides are associated with fine-grained marine sedimentary formations or weathered volcanic bedrock often found in regions experiencing rock uplift in the late Cenozoic, including portions of the United States, Taiwan, New Zealand, Europe, and Papua New Guinea (Putnam and Sharp, 1940, Keefer and Johnson, 1983, Baum et al., 1993; Zhang et al., 1993; Malet et al., 2002; van Asch 2005; Brückl et al., 2006; Rutter and Green, 2011; Daehne and Corsini, 2012; Di Maio et al., 2013; García-Davalillo et al., 2013; Simoni et al., 2013; Guerriero et al., 2014). In these areas, shearing and low-grade metamorphism associated with accretion often promotes low frictional strength of exhumed sedimentary bedrock. Mélange bedrock, which exemplifies many of these characteristics, has been identified in the mountainous regions of over 70 countries (Medley and Lindquist, 1995).

Weak mélange materials promote widespread slope failure through basal sliding and flow-like deformation that drives prodigious erosion despite modest (< 35%) slope angles. Erosion rates in earthflow-dominated regions approach and sometimes exceed 1.0 mm/yr, similar to rates from steep, bedrock-dominated settings (Zhang et al., 1993; Cerovski-Darriau et al., 2014). Unlike rapid bedrock landslides, however, earthflows do not evacuate completely upon failure but instead translate downslope continuously or episodically much like glaciers. Akin to glacial accumulation zones, the upslope margins of earthflows scavenge weathered material that coalesces midslope to form a coherent sliding mass much like a conveyor system (Keefer and Johnson, 1983) (Fig. 1). Upon reaching valley floors, earthflows tend to exhibit a lobate or 'toe'-like morphology that is often truncated by river incision in areas where hillslopes are coupled to the channel network. These primary physical characteristics (as well as secondary features such as gullies and fractures) of earthflow landslides are advantageous because the morphologic signature of active or relict sliding can often be readily identified (Keefer and Johnson, 1983). In addition, because earthflows tend to remain active for long periods of time (>100 years) (Skempton et al., 1989; Bovis and Jones, 1992; Varnes and Savage, 1996; Schulz et al., 2009a; Mackey et al., 2009), they afford the opportunity to document how slide velocity varies over a broad range of timescales (i.e., 10^0 to 10^9 sec).

In this contribution, we summarize and synthesize our on-going efforts to quantify landslide controls on landscape evolution in a rapidly uplifting section of the Eel River basin in the

Northern California Coastal Ranges. The ubiquity of active slope failures in this area underlain by accretionary bedrock of the Franciscan Complex, a notoriously failure-prone geologic unit, provides an ideal natural laboratory to study the temporal and spatial patterns of slope instability. High-resolution topographic data derived from airborne lidar provides essential morphologic information and when coupled with datasets on landslide dynamics from remote sensing, our analyses provide a spatially explicit means to pinpoint and tally landslide contributions to denudation in space and time. While landsliding is often identified as the primary erosional process in mountainous settings, few studies have documented how tectonic forcing controls the frequency of landsliding and the tendency for erosion to balance rock uplift. Our research also informs the development, calibration, and testing of physically-based models to interpret and predict landslide response to tectonic and climatic variations. In particular, we demonstrate how our findings can be used to establish the functional relationships that underlie the threshold slope model, such as the variation of landslide frequency (or areal density) and hillslope angle with erosion rate.

2. Study area: Eel River Canyon, Northern California

2.1. General background

The Northern California Coast Ranges are comprised of the Franciscan Complex, a Jurassic-Cretaceous, pervasively sheared, meta-sedimentary accretionary prism complex subject to uplift since the Neogene (Fig. 2). Annual rainfall averages 1.4 m, primarily falling between October and May. The combination of weak lithology, active tectonics, and seasonal rainfall makes the Eel River watershed especially prone to landslides and slope instability, and an ideal location to study active earthflow processes (Fig. 3).

2.2. Geological context

The Franciscan Complex is comprised of three structurally separated lithologic belts, the Eastern, Central and Coastal belts. These terrains are younger to the west, reflecting the cumulative accretion of oceanic sediments to western North America (Jayko et al., 1989; McLaughlin et al., 2000). The Central belt is especially prone to landsliding as it consists of an extensive Late Jurassic to Middle Cretaceous argillaceous mélange, which is broadly defined as a mixture of relatively strong inclusions (blocks) of sandstone, chert, and shale, ranging in size between sand grains and mountains (i.e., 10^{-2} to 10^{4} m), embedded within a weaker matrix of sheared argillite, shale, or siltstone (Fig. 4). This assemblage was obducted to North America from 88 to 40 Ma, prior to emplacement of the Coastal Belt (McLaughlin et al., 2000).

Furthermore, large blocks of older, meta-sandstone, meta-basalt and high-grade blueschist rocks may have been incorporated into the Central belt from the older Eastern belt during oblique dextral translation, although alternative emplacement histories are possible. These more competent lithologic units have a significant local influence on the topography, manifesting as topographic highs amid the argillaceous units and mélange. The mélange bedrock favored open oak grassland at the time of European settlement in the 1850s, attracting ranchers, and the primary land use remains low-density cattle ranching. Conifer growth and forestry are generally limited to isolated outcrops of sandstone or other resistant bedrock.

The western North American plate boundary switched from subduction to strike-slip in the Oligocene with the formation of the San Andreas fault. Since this transition, the post-emplacement tectonics of the Northern California Coast Ranges has been dominated by the northerly migration of the Mendocino triple junction (MTJ) at 5 cm/yr, which is reflected in the northwest trending structural grain that dominates the modern topography, with major axial drainages and ridges trending northwest (McLaughlin et al., 1982) (Fig. 2). The Pacific and Gorda plates are translating north relative to North America, creating the San Andreas Fault to the south (Furlong and Schwartz, 2004). Numerical models that account for the change in lithospheric thickness, heat flow, and isostatic adjustment predict a zone of rapid rock (>1 mm/yr) uplift that migrates north at approximately 5 cm/yr (Furlong and Govers, 1999; Lock et al., 2006) and a series of northwest-trending emergent fault systems cut through the Northern California Coast Ranges associated with the advance of the MTJ (Kelsey and Carver, 1988). This migrating zone of uplift has had a profound influence on the landscape, causing river capture and drainage reversals. Most notably, the headwaters of the Russian River were captured by the Eel River at 2 Ma when river incision was unable to keep up with the transient wave of increased uplift rates (Lock et al., 2006), generating 'fish hook' drainage patterns in several Eel River tributaries.

2.3. Rates of rock uplift and erosion

Rates of uplift and incision in the region are primarily constrained by analysis of fluvial and marine terraces. Merritts and Bull (1989) and Merritts (1996) documented variable rates of coastal uplift peaking at 5 mm/yr along the coast near the inland projection of the MTJ. These high rates are proposed to be highly localized, however, and are associated with the rapid exhumation of a narrow, accreted terrane termed the King Range (Dumitru, 1991). Further inland, uplift rates at this same latitude (40-41°) are modeled to approach 1 mm/yr along the Eel

River corridor near Alderpoint (Lock et al., 2006) (Fig. 5), although direct constraints on exhumation are sparse and do not correspond with our field area (Dumitru, 1991; Batt et al., 2010). Further south, rock uplift is thought to decrease according to predicted surface deflections from the Mendocino Crustal Conveyor (MCC) geodynamic model (Furlong and Govers, 1999; Lock et al., 2006). Our review and synthesis in this contribution focuses on the zone of rapid uplift along the Eel River corridor, roughly coincident with the inland projection of the MTJ and within the Franciscan Complex (Fig. 2).

The Northern California Coast Ranges have received significant attention by geomorphologists because of the high erosion rates that have been documented since the 1960s. Wahrhaftig and Curry (1967) warned that rates of erosion in the Eel River were abnormally high in comparison to other North American river systems, and called for further research into sediment sources and monitoring. After an intensive period of hydrologic and suspended sediment data collection by the USGS in the mid-20th century, Brown and Ritter (1971) established that from 1957 to 1967, the Eel River had the highest annual sediment yield of any non-glacial, continental river in the United States at 10,000 tons per square mile (3900 tons/km^2). Wheatcroft and Sommerfield (2005) re-analyzed suspended sediment data (1960-1980) and calculated a sediment yield of 2200 tons/km^2/yr, which equates to a catchment averaged erosion rate of 0.9 ± 0.3 mm/yr assuming a bedrock density equal to 2.5 kg/m^3. Extensive research has also been performed in the offshore environment focusing on the rate and distribution of shelf sedimentation (e.g., Nittrouer, 1999). Notable are the changing rates of sedimentation over the Holocene and late Pleistocene (Syvitski and Morehead, 1999; Sommerfield and Wheatcroft, 2007) and in historical times (Sommerfield and Nittrouer, 1999; Sommerfield et al., 2002). During the 20th century, shelf sediments attributed to the Eel River show an increase during the second half of the century, coincident with widespread logging and road building as well as major storms in 1955 and 1964 (Brown and Ritter, 1971; Sloan et al., 2001; Sommerfield and Wheatcroft, 2007).

Long-term (pre-historic) rates of erosion in the Eel River Basin established using cosmogenic radionuclides are consistent with modern records. North of the zone of highest predicted rock uplift, Ferrier et al. (2005) used cosmogenic isotopes in stream sediments from Redwood Creek to estimate erosion rates of 0.14 to 0.44 mm/yr. Similarly, Balco et al. (2013) measured cosmogenic catchment-averaged erosion rates of 1.1 ± 0.15 mm/yr in the upper Van Duzen River and 0.6 ± 0.07 mm/yr in the Eel River upstream of Scotia. Both of these locations coincide with the region of high predicted uplift rates (Lock et al., 2006). To the south, near the

headwaters of the Eel system (and coincident with terrain well south of the locus of rapid uplift associated with the MTJ), Fuller et al. (2009) and Willenbring et al. (2013a) used cosmogenic isotopes to calculate erosion rates for the upper South Fork Eel River and obtained values ranging from 0.2 to 0.5 mm/yr.

2.4. Landslide investigations

Our study focuses on a section of the mainstem Eel River between Dos Rios and Alderpoint (Figs. 2 and 5), which has one of the highest concentrations of earthflow activity in the Eel River catchment (Brown and Ritter, 1971) and coincides with the inland projection of the MTJ and thus resides within the predicted zone of rapid uplift (Lock et al., 2006).

Kelsey (1977, 1978, 1980) performed extensive landslide studies in the Van Duzen river basin, a large tributary of the Eel River just south of Humboldt Bay. During the 1970s, Kelsey used field surveying and aerial photos to quantify displacement and calculate a sediment budget for 19 active earthflows. He found that while active landslides covered just 1% of the Van Duzen basin area, these features contributed 10% of the sediment in the channel network over the period of monitoring. Furthermore, Kelsey (1980) estimated that earthflow translation accounts for approximately 50% of the sediment flux from active features, the remainder being extricated by active gullies on the surface of the earthflow. Kelsey (1980) and Muhs et al. (1987) highlighted the role of contrasting geomorphic processes operating in different rock types within the Franciscan Complex. The harder, competent, sandstone blocks feature well organized ridge and valley drainage networks, with erosion dominated by fluvial and debris flow incision. In contrast, the weaker mélange units have a poorly developed ephemeral drainage network and long, low-gradient slopes due to earthflow and other mass movement processes. Despite this weak lithology, rivers sometimes steepen when they cross particular reaches, as earthflows deliver boulders to the channel which armor the bed (Kelsey, 1977, 1978).

Further north in the Redwood Creek catchment, USGS scientists quantified many aspects of sediment production and transport (e.g., Harden et al.,1995; Nolan and Janda, 1995). Nolan and Janda (1995) monitored the sediment flux from two Redwood Creek earthflows, but concluded overland flow and gully processes accounted for only 10% of the long term erosion of the earthflow complex, the majority coming from mass movement. They also stressed the spatial variability of earthflow activity across Northern California, due to lithology and the complex evolution of individual earthflows. Iverson (1986a, 2005; Iverson and Major, 1987)

studied the Minor Creek earthflow in the Redwood Creek Basin and developed a numerical model to decipher seasonal earthflow movement by the slow infiltration of winter rainfall through the landslide mass. More recently, Iverson (2005) used Minor Creek data to argue that earthflow movement may be regulated by shear zone dilatancy, which can decrease pore pressures, thus preventing catastrophic failure.

Large landslides and earthflows along the Eel River canyon between Dos Rios and Alderpoint were addressed by engineering reports for the California Department of Water Resources (Dwyer et al., 1971; Scott, 1973; Smith et al., 1974) in anticipation of dam construction to supply water to the city of Los Angeles (California Department of Water Resources, 1965). These reconnaissance studies with descriptions and analysis of the landslides included back-of-the-envelope estimates of landslide-generated sediment flux and some limited information on slide depth and long term movement rates. Combined with burgeoning public pressure in Round Valley (Simon, 2001), the immense cost and hazard associated with dam construction and maintenance in highly landslide-prone terrain persuaded the Bureau of Reclamation to abandon their massive reservoir scheme. The Northwestern Pacific Railway follows the main stem Eel River canyon, connecting Eureka to San Francisco, but this line was abandoned in 1998, partially due to the high cost of landslide related maintenance.

Otherwise, very little data exists on the depth of large landslides and earthflows along the Eel River. The exceptions are two landslides in the lower reaches of the Middle Fork Eel River (California Department of Water Resources, 1970), approximately 34 km southeast of our study area, but in comparable Central belt Franciscan lithology. Boreholes in the 1.6 km long, 0.45 km^2 Salt Creek landslide, 3.5 km upstream of Dos Rios, demonstrate that landslide material thickens from 6.7 m near the headscarp to 33 and 35 m near the toe. A borehole in the ~1 km-long Salmon Creek landslide, 16 km upstream from Dos Rios, was sheared off at 34 m depth, although the inclinometer also revealed slow deformation at 57 m, attributable to deep seated failure within the sheared shale bedrock. Malhase (1938) described an Eel River landslide that was coined the 'Mile 201' slide after a wet winter in 1938: "The surface of the slide takes on the characteristic form of mud glaciers, with lateral terminal moraines, with rolls and pressure ridges forming valleys and hummocks. Great cracks open up into which water from the surface enters."

3. Key findings

11

In this section, which constitutes the core of this contribution, we review and synthesize our key findings for the rapidly eroding Eel River Canyon that have emerged since 2005. In addition, we present a small but not insignificant suite of new datasets and analyses that augment and extend our previous work. Taken together, this suite of studies reveals the dynamics of landsliding and related surface processes in a region of rapid uplift and erosion. In essence, we seek to characterize the temporal and spatial scales across which landslides exhibit systematic (and potentially predictable) behavior in order to facilitate modeling for human and geologic timescale applications. Put simply, we endeavor to document how landslides enable a mountainous landscape to accommodate (and balance) rapid uplift.

3.1. Landslide mapping and inventory

A first-order, but non-trivial, task is to document the distribution of active earthflows. Even when dormant, earthflows can retain the morphologic features of movement for long periods of time (Fig. 1). Mapping active earthflows is therefore complicated because much of the landscape bears topographic features diagnostic of past generations of slope failure.

We tackled the problem of discriminating between dormant and active earthflows by using a high resolution airborne lidar dataset (acquired through NCALM) in concert with historic aerial photos (Mackey et al., 2009; Mackey and Roering, 2011) and satellite radar interferometry (Roering et al., 2009; Handwerger et al., 2013; Handwerger et al., in review). First, because shrubs and trees live on the surface of active earthflows, these markers can be discerned both in aerial photos and on unfiltered lidar images (Fig. 6). By identifying identical features in lidar and photos, we objectively mapped earthflows that were active between 1944 and 2006 and discriminated these portions of the landscape from stable terrain. Using morphologic features such as headscarps, levees or lobes, we defined the boundaries of flows identified as active and confirmed the activity status of many earthflows in the field (Fig. 6). This process requires high-resolution aerial photos (preferably high-resolution diapositive scans which are not subject to warping like photo paper). Once the historical photos were orthorectified using Leica Photogrammetry Suite, we were able to confidently distinguish displacements >3 m between successive photos (Mackey and Roering, 2011). When combined with the time interval between photos and/or lidar-derived images, this uncertainty value determines the threshold velocity of landslides that we can reliably detect. For example, we cannot confidently identify active landslides with velocities less than 0.3 m/yr given photo intervals of 9 years or less. Fortunately, however, long photo (or imager) intervals (e.g., 1944 to 2006) enable us to

confidently identify landslides with average velocities on the order of 0.05 cm/yr. Given that slower landslides are precluded from our analysis, our photo-derived landslide inventory represents a minimum estimate of active landslides.

Satellite-based InSAR (Interferometric Synthetic Aperture Radar) complements the air photo inventory by providing high-precision (<0.01 m) measurements of ground surface deformation with a short repeat interval (10^1 days; Bürgmann et al., 2000). Several studies have successfully used InSAR data to image landslide activity within the accretionary units of Western California (Hilley, et al. 2004; Roering et al., 2009; Calabro et al., 2010; Zhao et al., 2012; Scheingross et al., 2013; Handwerger et al., 2013). Our datasets were acquired by the PALSAR instrument on the ALOS-1 satellite, which operates with a 46-day acquisition interval and L-band (23.5 cm wavelength) antenna (Roering et al., 2009; Handwerger et al., 2013). In our study area, major ridge and valley axes are oriented such that the ALOS-1 satellite's line-of-sight (LOS) is roughly parallel to the downslope axis of many active landslides, which facilitates their detection. Additionally, the region lacks dense forest cover that complicates the use of InSAR in some mountainous regions (Fig. 3). Satellite track 223 frame 790 and track 224 frame 790 overlap portions of our field site, which effectively doubles the number of scenes available in these areas. We produced 165 differential interferograms between February 2007 and January 2011 with the Repeat Orbit Interferometry Package (ROI PAC) developed at JPL/Caltech (Rosen et al., 2004). Landslides were identified by stacking interferograms and using statistical analysis to reduce noise. We confirmed the location of each landslide using high resolution DEMs (1 and 10 m grid spacing).

From the historic air photo analysis (1944 to 2006), we identified 122 active earthflows covering 16.5 km^2 (~7%) of the 226 km^2 lidar study area (Mackey and Roering, 2011). The slide areas are log-normal distributed and have a median area of 3.65x10^4 m^2 and an interquartile range of 1.25x10^4 to 1.17x10^5 m^2. Our method enabled us to identify active slides as small as 2x10^3 m^2, although this lower detection limit also depends on the presence of surface markers or diagnostic features. Our landslide map also shows that individual active earthflows often deviate significantly from the classic hourglass earthflow model (Fig. 7). Many earthflows have complex and intricate margins and multiple small tributary earthflows that feed a centralized transport zone (Fig. 7). These geometries indicate that earthflows can bifurcate around resistant topography, promote ridge migration, and capture the drainage area of adjacent terrain. Typically, larger earthflows extend from channels to ridgelines, but smaller earthflows

13

sometimes occupy midslope locations, which suggests that earthflows may persist by colluvial loading from upslope. The largest active earthflow in the study site, the Boulder Creek earthflow (~5 km long and 3.1 km^2 in area), forms the axis of a small (15 km^2) tributary catchment. A channel named Boulder Creek bisects this earthflow, which suggests that the upper limit to earthflow size may be set by the competition between earthflow movement and channelized erosion. At the downslope end, earthflow toes form lobate features or truncated vertical faces depending on the frequency of channel activity.

From our InSAR inventory (spanning 2007–2011), we identified 50 landslides over a ~14,000 km^2 study area that encloses our lidar coverage (Fig. 5). These slides span two orders of magnitude in area (5.4x10^4 to 7.8x10^6 m^2) and 13 of the 50 were previously identified through our air photo analysis (Mackey and Roering 2011) (Fig. 5). Consistent with previous evidence for a strong lithologic control on active sliding (Kelsey, 1978), we observe that 97% of these InSAR-identified slides coincide with the slide-prone Central and Eastern belts of the Franciscan mélange. In the lidar coverage area, where our photo and InSAR inventories overlap, we note that large slides identified with the historical photos were also identified by the InSAR, but the InSAR analysis does not reliably detect some small narrow features given the spatial resolution (Fig. 8). Although powerful for detecting deformation patterns in space and time (see below), our current implementation of InSAR precludes it from providing a complete and robust landslide inventory in our study area for two reasons. First, radar interferometry is blind to surface displacement that is perpendicular to the satellite's line-of-sight (LOS). Given the ALOS satellite's north-northeast orbit (and east-northeast LOS), any slides whose axis orientation roughly coincides with the orbit direction will not be detected (Fig. 8). Additionally, our implementation of InSAR has difficulty resolving small slides (<5x10^4 m^2), which occupy only a few pixels of each interferogram. For these reasons, our InSAR-derived landslide inventory underestimates the area of active landsliding. Fortunately, however, SAR imagery can be processed in alternate modes, such as with automated cross-correlation pixel tracking (e.g., Cosi-CORR; Leprince et al., 2008), which can detect deformation parallel to the satellite orbit and thus increase our ability to resolve smaller slides with sub-optimal orientations. This mode of processing uses amplitude information (rather than phase imagery) and thus suffers from decreased accuracy such that slides must have substantial velocity to be detected. Even more promising, though, the recent and planned launch of new SAR satellites with shorter repeat intervals and higher resolution ensures that this technology will continue to improve landslide mapping capabilities (Bürgmann and Thatcher, 2013; Scheingross et al., 2013).

Given the limitations of our InSAR analyses in their current incarnation, we emphasize the photo-derived analysis of active sliding for the purposes of compiling a landslide inventory. While the Eel River system is commonly referred to as landslide-dominated, we estimate that no less than 7% of the lidar study area is subject to active sliding. Interestingly, the average axial slope of these active features is indistinguishable from that of proximal, inactive slopes (both average approximately 34%). So, in sum, while the vast majority of the landscape exhibits the morphologic signature of sliding and remarkably uniform slope angles, less than 10% of the land surface currently experiences perceptible activity. This discovery motivates us to determine the fluxes associated with active slides as well as determine other factors that might distinguish active and inactive hillslopes.

3.2. Historic landsliding and sediment production

After identifying active earthflows, our next task was to quantify their contribution to the sediment yield of our study area. Because annual rates of sliding can vary due to climate and other factors (Mackey and Roering, 2011), we sought to characterize their average pace to facilitate comparison with rates of uplift and erosion. For this analysis, Mackey and Roering (2011) focused on the photo-based landslide inventory because it offers the most comprehensive and long-term (>60 yr) depiction of active sliding albeit in a somewhat limited spatial domain (226 km^2 study area). As detailed in Mackey and Roering (2011), we used the displacement of features on the earthflows combined with measurements of landslide geometry to estimate sediment delivery to the channel network. Of the 122 active earthflow features, 62 directly entered a channel (or gully) and these connected or coupled slides account for ~6% of the study area (Fig. 7). We calculated the average annual sediment flux for each slide as the product of average slide velocity, slide width and slide thickness measured at the hillslope-channel interface from field observations and/or lidar analysis. Landslide thickness is notoriously difficult to estimate although recent advances hold promise (Booth et al., 2013).

From the 62 connected earthflows, we estimated an average sediment production rate of 1.2x10^5 m^3/yr which emanated from 13.6 km^2 of the 226 km^2 study area (Mackey and Roering, 2011). When this flux is attributed only to this area of active sliding, we estimate a landslide-specific sediment yield of 1.9x10^4 t/km^2/yr, or an equivalent bedrock erosion rate of approximately 7.6 mm/yr given a bedrock density 2.5 g/cm^3. This lowering rate is an order of magnitude faster than estimates of rock uplift and erosion in the region (0.3 to 1.0 mm/yr) which

15

suggests that when viewed in isolation, these active slides denude rapidly at an unsustainable pace. However, when this rate of sediment production is distributed over the entire lidar study area of 226 km^2, the slide-driven sediment yield is 1.1×10^3 t/km^2/yr (or equivalent to a bedrock lowering rate of 0.45 mm/yr), which coincides with the range of erosion and uplift rates estimated for the region. Furthermore, when compared to suspended sediment data collected along the Eel River near Scotia, CA, we discovered that slide-derived sediment accounts for more than half of the catchment flux (Wheatcroft and Sommerfield, 2005). Thus, our data can be interpreted in two key ways: 1) landslides constitute the primary erosional process in the Eel River, and 2) erosion rates for the Eel River are similar to predicted rock uplift rates implying the potential for an approximate balance and steady state topography.

Although steady-state interpretations have been established for many landscapes (Hovius et al., 1997; Meigs et al., 1999; Larsen and Montgomery, 2012), additional constraints in our study area enable us to estimate the frequency with which landslides 'migrate' across the landscape in order to keep pace with uplift. Specifically, observed earthflow velocities (0.5 to 2 m/yr) as well as meteoric [10]Be profiles on an active earthflow have been used to estimate an average earthflow residence time of 1.5 kyr (Mackey et al., 2009; Mackey and Roering, 2011). Combined with our finding that ~7% of the landscape experiences slope instability at a given time, this residence time suggests that the recurrence interval for sliding at a given hillslope location is 21,000 yr. For this calculation, we estimated recurrence interval as the average residence time for an individual landslide (1.5kyr) divided by the areal density of active sliding (in this case 7%). This frequency of landscape sculpting by slope failure accounts for the abundance of ancient landslide features with varying states of dormancy; in other words, the morphologic signature of past earthflow activity persists for $>10^4$ yr. In addition, the uniformity of slope angles, particularly the similarity for active landslides and inactive slopes, implies that sliding must propagate across the landscape with sufficient frequency to prevent the emergence of morphologic discontinuities that reflect the time since last failure. In other words, active landsliding revisits each locale in the landscape often enough to maintain uniformly graded slopes (Strahler, 1950). Lastly, our estimation of the frequency with which landslides 'repave' hillslopes also explains the relative paucity of Late Pleistocene fluvial terraces (or shorelines) in the Eel River corridor (Mackey et al., 2011) as these features have been almost wholly obliterated by sliding.

3.3. Automated landslide velocity analysis

Our analysis of slide-driven sediment production in Mackey and Roering (2011) is localized whereas a regional-scale landslide inventory for comparison with tectonic models will require a substantial increase in the area mapped. Manual feature mapping is labor intensive and because many slides have limited tree coverage, manual feature tracking can have limitations, potentially leading to an underestimate of sediment production values. Recent advances in image processing and comparison can automate the identification of changes between successive images. These techniques have the advantage of allowing images (e.g., successive orthorectified aerial photos) to be compared rapidly and objectively. Additionally, because image matching algorithms rely on transformation (e.g., Fast Fourier Transformation) of local patches of terrain rather than discrete features, they can quantify movement in regions of an earthflow that may be devoid of discrete markers. The software module COSI-Corr uses precise orthorectification (Ayoub et al., 2009) to identify changes in sequential images at the sub-pixel scale (e.g., Leprince et al., 2008). By comparing rectified aerial photos of the same area from different times, COSI-Corr can identify areas of continuous displacement.

In a new analysis, we used the COSI-Corr algorithm to estimate displacements across the Boulder Creek earthflow using photos taken in 1964 and 1976 (Fig. 9). The displacement field is very similar (within 10%) to that generated from the InSAR analysis and manual tree tracking (specifically, the fastest rates occur in the transport zone and movement of the toe is minor), but our COSI-Corr result boasts a relatively continuous deformation as displacement vectors are generated where they could not be manually identified (Fig. 9). This analysis is particularly useful for quantifying the orientation of earthflow fluxes proximal to axial and lateral gullies, which serve to transport earthflow-prone material into the fluvial network. In particular, Fig. 9 shows diverging displacement vectors along the northern margin of the earthflow that constitute sediment delivery into the gully network. Unfortunately, in the upper (branching) reaches of the earthflow, large displacement gradients and surface disruption preclude robust resolution of displacement in some zones. Nonetheless, this technique promises to facilitate quantification of landslide kinematics through the use of archival imagery, including air photos and troves of declassified optical satellite imagery (e.g., Hollingsworth et al., 2012).

3.4. Gully-landslide interactions

Our velocity and sediment production analysis does not explicitly account for gully networks that often become etched atop active earthflows and may contribute to landslide kinematics and sediment production (Roering et al., 2009; Handwerger et al., in prep). During significant rainfall

events, these sometimes discontinuous gullies convey overland flow with high concentrations of suspended sediment (Kelsey, 1978). To assess the relationship between gullies and earthflow features in our study area, we used the lidar data to apply a drainage area threshold and map gully networks as pixels with area between $3{\times}10^3$ and $1{\times}10^6$ m^2 (Fig. 10). According to this new analysis, the resulting gully network corresponds well with field observations generated for several earthflows, but more importantly, zones of high gully density exhibit a strong association with active or dormant earthflows (Fig. 10). At least two factors may be responsible for this association: 1) earthflows tend to occur in topographically convergent terrain, which favors overland flow, and 2) surface disruption due to landsliding (such as fractures and broken ground) reduces the ability of vegetation and soil sealing to resist shear stresses imposed by overland flow. In some cases, examination of the historical imagery shows significant expansion and evolution of gully networks as earthflow motion can close and/or reorient gullies. Field observations indicate that gully systems rarely attain depths greater than 5 m (with the exception of Boulder Creek that has incised the Boulder Creek earthflow > 40 m) and thus are unlikely to intersect the basal sliding surface (Handwerger et al., 2013). In the vast majority of gullies atop active slides, the channel beds are lined with coarse boulders that appear to originate from upstream transport as well as local bank failure. We often observe that boulders accumulate and form interlocking structures and armored beds that appear to limit further channel incision. As a result, gully incision on earthflows may be subject to a negative feedback as incision increases the delivery of coarse sediment from the adjacent banks. Combined with the influence of on-going landslide movement, these processes contribute to the ephemeral nature of these features.

In the absence of suspended sediment data for gully systems, we have limited ability to assess their contribution to the sediment budget of our study area. Our earthflow flux calculations, however, may incorporate some component of gully erosion because these slot-like features are not accounted for in our measurements of earthflow depth and width. In order words, our 'plug-flow' characterization of earthflow transport may indirectly include fluxes associated with gully dissection because we do not subtract these gully volumes from our analyses. By contrast, however, gullies can extend upslope into the amphitheater-like landforms above earthflows and sediments emanating from these areas are not included in our current analysis. Most generally, the tight coupling of earthflow and gully systems in our study area motivates future investigations to explore feedbacks between gully incision and slope movement that may influence sediment yield and dictate long-term patterns of hillslope evolution.

3.5. Knickpoints, landslides, and cosmogenic radionuclide erosion rates

In recent decades, in-situ cosmogenic radionuclides (CRN) analyzed in modern stream sediments have become a staple for geomorphic studies seeking to decipher how erosion rates depend on topography, climate, tectonic forcing, and rock type (e.g., Portenga and Bierman, 2011; Granger et al., 2013; Willenbring et al., 2013b). This method accounts for total denudation of the land surface and thus integrates the erosional contributions of earthflows, gullies, soil creep, and other processes. Here, we present a new analysis of cosmogenic erosion rates for a major tributary (Kekawaka Creek) in our study area that exhibits a substantial knickpoint separating somewhat gentle headwaters terrain from steep channels coupled to active landslides in the lower portions of the catchment. This configuration implies that the upper portion of Kekawaka Creek is essentially isolated from the regional uplift/erosion rate and thus provides an opportunity to analyze how incision regulates hillslope gradients as well as active sliding and erosion rates.

Although the paucity of quartz-bearing sediments limits the application of in-situ cosmogenic radionuclides in some earthflow-dominated landscapes (Reusser and Bierman, 2010), meta-sandstone blocks (often termed knockers) crop out in sufficient abundance in many Northern California catchments, generating readily sampled quartz-rich stream sediments. Resistant, quartz-rich clasts smaller than 10 m often emerge within earthflows while larger clasts (up to km-scale) can form promontories of sufficient size to deflect earthflows and anchor prominent peaks. In stream channels, clasts <0.5 m in diameter are subject to frequent fluvial transport and are thus likely to account for the majority of modern sand and gravel in stream sediments used for cosmogenic radionuclide analysis.

Knickpoints often regulate the adjustment of fluvial networks to baselevel changes driven by tectonic forcing and in the Eel River system many tributaries harbor substantial knickpoints that arise from large (>10 m) resistant bedrock clasts that are composed mostly of sandstone, but also greenstone and chert (Figs. 3 and 4). Along the main stem of the Eel River, we observe no major boulder-derived knickpoints owing to the wide channel and high discharge. By contrast, knickpoints composed of megaclasts within tributaries are common and emerge locally or through downslope transport within earthflow bodies as noted by Kelsey (1977). Regardless of the pathway, the impressive resistance of these clasts guarantees their persistence in the fluvial network for long timescales (>10^5 yr). In Kekawaka Creek, our lidar dataset reveals a large

knickpoint zone that separates the gentler (average slope = 23%) upper catchment with a paucity of active slides from the steeper lower catchment (average slope = 30%) that features at least five active landslides each exceeding 1 km in length (Fig. 11). In a new analysis, we sampled Kekawaka stream sediments for CRN analysis about 100 m upstream of the junction with the Eel River as well as near the upstream extent of the steep, boulder-dominated reach that defines the knickpoint zone (Fig. 11). We processed stream sediments with 0.25 to 0.5 mm median diameter at the University of Washington Cosmogenic Nuclide Laboratory following the techniques described in Balco et al. (2013) and references therein (Table 1). Because the lower catchment sample incorporates sediments from both the lower and upper catchments, we used the mixing model described in Granger et al. (1996) to calculate independent erosion rates for the upper and lower portions of the catchment (Table 1).

According to our CRN analyses, erosion rates above the knickpoint zone average 0.29 ± 0.05 mm/yr, while erosion rates for the lower reaches of Kekawaka Creek average 0.76 ± 0.11 mm/yr (Fig. 11). The lower catchment erosion rate is similar to values established by suspended sediments (Wheatcroft and Sommerfield, 2005) as well as cosmogenic erosion rates in the nearby Van Duzen River (Balco et al., 2013). Given the >2x erosion rate difference and the relatively subdued topography and wide valley floors in the upper reaches of the catchment, we postulate that Kekawaka Creek is increasing in relief. The multitude and magnitude of boulders composing the knickpoint zone within Kekawaka Creek suggest that these features are long-lived such that large, infrequent resistant blocks within the mélange likely have a disproportionate influence on river channel evolution and regional relief. The lower portion of the catchment exhibits active earthflows, and although the upper catchment exhibits some marginal morphological evidence of dormant landslide features, neither air photo nor InSAR analyses revealed evidence for active landsliding in the upstream reaches. This suggests that the frequency of active earthflows is highly sensitive to the pace of channel incision. More specifically, the slow-eroding upper catchment may require relatively infrequent sliding in order to denude at the observed rate of just under 0.3 mm/yr. At this erosion rate, the combination of gully erosion and soil creep may be able to generate sediment with sufficient pace, whereas increases in incision would likely promote earthflow contributions with increased frequency.

3.6. Erosion from topography: Slope evolution model with landsliding
To interpret our Kekawaka erosion rate and topographic data with a mechanistic approach, we invoked the predictions of a 1-D model for hillslope evolution subject to slow-moving landslides

(Booth and Roering, 2011). Essentially, we seek to establish and calibrate a functional relationship between topography (average slope angle, in this case) and erosion rate. In a given setting, topography-denudation studies frequently demonstrate that average slope (or mean local relief) accounts for a significant amount of the observed variance in erosion rate values (e.g., Ahnert, 1970; Larsen et al., 2014). Specifically, erosion rate and average slope are often positively correlated, but this linear relationship tends to break down when slope angles approach threshold values and small increases in steepness generate large increases in erosion rate (Montgomery and Brandon, 2002). This threshold regime has been observed in numerous settings, including the San Gabriel Mountains, the Himalayas, and other active orogens which are dominated by steep, bedrock hillslopes (Montgomery and Brandon, 2002; Binnie et al., 2007; Ouimet et al., 2009; DiBiase et al., 2010). These topography-denudation relationships are consistent with the predictions of a nonlinear sediment transport model that accounts for rapid increases in flux at steep angles (Andrews and Bucknam, 1987; Roering et al., 1999; Roering et al., 2007) such that slope angles become independent of erosion rate in steep terrain. The universality of such relationships and in particular their application to earthflow-prone terrain, however, has not been tested.

Our physically-based hillslope evolution model assumes that earthflows behave similarly to glaciers (Glen, 1955). Specifically, it states that the shear deformation rate is a power law function of the driving shear stress with a stress exponent greater than one (Booth and Roering, 2011; Booth et al., 2013). This is consistent with plug-flow velocity profiles from earthflows and other slow moving landslides around the world, where shear deformation is concentrated in a basal layer ranging from millimeters to meters in thickness, and material nearer the surface translates as a rigid block (Vulliet, 2000; Casson et al., 2005; Coe et al., 2009). Iverson (1986a,b,c) first assumed this type of rheological model for slow moving landslide deformation, while Vulliet and Hutter (1988a,b,c), and Vulliet (2000) demonstrated that the flow law exponent ranged from 1 to 15 at a variety of sites. An exponent of 1 indicates linear viscous flow, while exponents greater than 1 indicate an increasing degree of plug flow approaching a rigid sliding block. In addition, our model incorporates the influence of gully erosion and soil creep on average hillslope gradients using previously published transport laws (Booth and Roering, 2011).

The form of slide-prone slopes in our study area records topography-erosion feedbacks integrated over time scales (1 to 5 ka) similar to cosmogenic erosion rate timescales (~1 ka). In

other words, the link between topographic form and cosmogenic erosion rates allows us to constrain hillslope erosional processes well beyond historical timescales. Assuming steady erosion of a given hillslope, our model predicts landslide erosion dominates the hillslope response at high rates of erosion such that $S \sim E^{(1/p)}$, where S is the mean slope, E is the erosion rate due to earthflows, and p is the stress exponent in the power law rheology (Booth and Roering, 2011). At lower erosion rates, the relationship between mean slope and erosion rate follows a different scaling exponent, n, (i.e., $S \sim E^{(1/n)}$) that reflects how gully erosion depends on the average gully slope in a similar fashion (n is typically ~1). In other words, our model predicts that a log-log plot of erosion rate versus average slope angle exhibits a kink that separates two power-law regimes with scaling exponents of p and n, assuming a significant difference in the values of p and n. The erosion rate that coincides with the transition between these two regimes varies with process law parameter values and has not been quantified for a real landscape (Booth and Roering, 2011).

Currently, we have limited erosion rate data to calibrate and test a landslide topography–erosion relationship. If we assume that erosion in both the upper and lower portions of Kekawaka Creek is dominated by landsliding, such that slope and erosion rate follow the 1/p scaling, our data indicate that p is 3.7, consistent with observations of thin shear zones and velocity profiles for similar earthflows in other settings (Booth and Roering, 2011). In this scenario, landsliding would dictate erosion in the upper catchment but at a frequency that is undetectable over historic timescales with our remote sensing analysis. Alternatively, given the paucity of active landsliding in the upper catchment, the observed erosion rate of 0.29 mm/yr may reside in the regime wherein erosion is accommodated primarily by gullying and soil creep and slope angle scales with erosion rate as 1/n. In this scenario, our limited erosion dataset precludes us from uniquely constraining parameter values that relate slope and erosion rate. Although unsatisfying, this interpretation is appealing given the lack of landslides in the upper catchment and the abundance of active sliding in the lower section. Thus, the erosion rate that coincides with the transition between the non-slide and slide-dominated erosion-slope angle scaling would be bracketed by our observed rates of 0.29 and 0.76 mm/yr. Additional data are required to further refine and test this interpretation, but these results suggest that from topographic data our model can be calibrated to interpret how both process and form respond to changes in erosion rate (Booth and Roering, 2011; Booth et al., 2013).

3.7. Seasonal dynamics: Landslide velocity

When averaged over long timescales (>10 yrs), individual earthflows in our study area tend to exhibit relatively consistent velocities (Mackey and Roering, 2011), suggesting that they persist in a chronic state of failure. By contrast, when examined over hourly to monthly timescales, notable field-based studies have shown that fluctuations in earthflow velocity are substantial (often greater than 50%), reflecting the influence of individual storms, seasonal and decadal rainfall patterns, and fluctuations in atmospheric pressure that drive changes in pore pressure along basal surfaces (Iverson and Major, 1987; Malet et al., 2002; Coe et al., 2003; Schulz et al. 2009b). The extent to which these historical timescale variations influence the long-term evolution of slide-prone landscapes is uncertain. For example, do seasonal fluctuations in velocity simply represent variations around long-term trends OR do sub-annual patterns have a cumulative effect on hydrologic-mechanical interactions that modulate the evolution of landslides, including their propensity to fail catastrophically? The tendency for earthflows in our study area to resist catastrophic failure is a critical characteristic that allows for the persistence of rapidly eroding, low-gradient topography. To document sub-annual landslide dynamics for the purpose of assessing landslide mechanics, Handwerger et al. (2013) performed a detailed time series analysis for a subset of slides in the InSAR landslide inventory discussed above.

Deep-seated slow-moving landslides typically require long (weeks to months) periods of precipitation in order for pressure changes to occur in the subsurface (Iverson and Major, 1987). Field-based studies have shown that pore-water pressure can diffuse from the surface through the landslide body and be represented with a simple one-dimensional linear diffusion equation (Iverson and Major, 1987; Haneberg, 1991; Reid, 1994; Iverson, 2000; Berti and Simoni, 2010, 2012). This model suggests that the time required for landslides to respond to rainfall (i.e., landslide response time) should vary with the thickness and hydraulic properties of each landslide. Thus, in regions with similar climate, soil properties, and topographic slopes, landslide response time should scale with the square of landslide thickness.

We quantified seasonal slide velocity patterns for 10 active earthflows by inverting 51 small-baseline interferograms using the method of Schmidt and Bürgmann (2003) and by combining both satellite tracks to achieve a temporal sampling as short as ~30 days (rather than 46 days for a single track) in certain time periods (Handwerger et al., 2013). These 10 landslides have areas ranging from 0.16 to 3.1 km^2 and average thicknesses of 8 to 40 m (Handwerger et al., 2013). Between 2007 and 2011, each slide displayed seasonal velocity changes that were remarkably similar in timing and magnitude despite a fivefold variation in slide depth (Fig. 12).

Each slide accelerated within 40 days of the onset of seasonal rainfall each fall before velocities peaked in mid-winter and decreased through the spring and summer. However, we are unable to resolve shorter onset times given the temporal resolution of the data. Observations of similar response times irrespective of landslide size appear to contradict a parsimonious implementation of the depth-dependent diffusion model. In Handwerger et al. (2013), we explored possible explanations for these observations. First, we used a 1D diffusion model with a range of hydraulic diffusivities measured at the nearby Minor Creek landslide (Iverson and Major, 1987) to show that negligible pore-water pressure changes likely occur in the deepest slides within 40 days of rainfall commencement. Among the possible explanations for the short and consistent onset times of the deepest slides is that field-based values of hydraulic diffusivity may underestimate the effective hydraulic diffusivity because field estimates are often derived from monitoring sites that are selected to avoid heterogeneities (e.g., large open mode deformation cracks) that facilitate rapid pressure transmission. In addition, like many hydraulic parameters, the effective diffusivity may scale with landslide size such that larger landslides exhibit high diffusivity values. Curiously, tracer studies show that hydraulic diffusivity values for mass transport vary as a power law function of transport length scale (Neuman, 1990; Gelhar et al., 1992) and the scaling exponent is often estimated to be between 1 and 2. If landslide thickness is considered the effective length, these scaling relationships could potentially account for our inability to detect a scale-dependent difference in landslide response time. In other words, if the effective hydraulic diffusivity of our landslides increases with length scale, larger (and thicker) slow-moving landslides may respond over a similar timescale as smaller (and thinner) ones due to scale-dependent hydraulic properties that dictate pore pressure dynamics. Unfortunately, however, these scaling relationships are derived for tracer data and thus far have not been established for pressure changes, which is more relevant for our purposes. Alternatively, our results may suggest that a simple 1D diffusion model may fail to characterize the multi-dimensional mechanical-hydrologic interactions that modulate the dynamics of an evolving earthflow. More generally, our analyses challenge us to: 1) increase the sampling frequency of our landslide time series with InSAR datasets, and 2) assess the hydrologic and mechanical processes that control the seasonal deformation of slow-moving landslides.

3.8. Seasonal dynamics: suspended sediment transport

Because our InSAR analysis suggests that the timing of seasonal landslide acceleration, peak velocity, and deceleration is similar across our study area, we anticipate implications for the timing of sediment delivery to the channel network. The predominantly fine-grained lithology of

the Franciscan Complex (notwithstanding the presence of resistant clasts) favors suspended load transport of earthflow-derived sediment. Thus, in addition to providing an estimation of catchment-averaged erosion on historic timescales, suspended sediment records may reveal the signature of seasonal earthflow activity when examined in detail.

Power-law relationships between discharge and sediment concentration are often used to generate sediment rating curves and estimate cumulative suspended sediment yields and thus erosion rates (e.g., Syvitski et al., 2000; Cohen et al., 2014). In many cases, sediment rating curves reveal a systematic and non-unique relationship between river discharge and sediment concentration. In other words, for a given river discharge, sediment concentration values exhibit variability that is not solely due to uncertainty or statistical noise (Walling and Webb, 1996; Hicks et al., 2000). Rather, discharge-concentration data can reveal sediment supply limitations whereby sediment concentrations drop to negligible values for discharges that previously exhibited measurable suspended sediment concentrations, or hysteresis whereby sediment concentrations for a given discharge in the rising limb of a hydrograph are greater than those corresponding the same discharge during the falling stage (Lopes and Ffolliott, 1993; Hovius et al., 2000). In a new analysis, we analyze suspended sediment records for the Eel River, anticipating systematic deviations in the discharge-concentration data that result from the mid-winter acceleration of earthflows and the delivery of fine-grained sediment to the channel network.

From 1960 to 1980, the US Geological Survey measured daily river discharge and suspended sediment concentration for the mainstem of the Eel River near the town of Scotia. While the data have been used to estimate sediment export and erosion rates (Wheatcroft and Sommerfield, 2005; Lock et al., 2006), the data also reveal inter-annual variability that presumably relates to variations in precipitation. In particular, a series of intense storms with a recurrence interval greater than 100 years occurred in 1964 and liberated enormous quantities of sediment across Northern California leading to extensive valley aggradation (Brown and Ritter, 1971). Similar to sediment rating curve changes observed after volcanic eruptions (Major, 2004), the 1964 event heavily perturbed the relationship between river discharge and suspended sediment concentration for several years following the storm.

In order to avoid the legacy of the 1964 event and isolate the signature of earthflow-driven sediment delivery, we analyzed suspended sediment data from 1960 to 1963 and 1970 to 1980.

In addition, following Wheatcroft and Sommerfield (2005), we culled data during low-flow conditions when sediment concentrations are contaminated by authigenic organic material such as diatoms. To do this, we plotted log-transformed daily discharge values (Q_w) and noted a bi-modal distribution with the higher peak associated with winter events and the lower peak associated with low-flow summer conditions. The discharge associated with the minimum between the two peaks reasonably separates these two regimes and thus we trimmed data with $\log(Q_w) < 1.55$ (or $Q_w < 35$ m^3/s). After this filtering, the 14-year record contains >4000 data points and reveals a distinctive discharge-concentration relationship that is not well described by a single power-law equation (Fig. 13A). We used a locally weighted scatterplot smoothing (LOWESS) algorithm following Major (2004) to fit the discharge-concentration data and calculated the residuals. Surmising that the residuals vary seasonally because of lagged earthflow activity, we plotted residuals as a function of water day (defined as October 1 = 1 and September 31 = 365) for the aggregated 14-year dataset. Similar to other studies, the data exhibits hysteresis, which in our case is reflected by decreasing residual values through the water year. Specifically, we observe positive residuals early in the water year that progressively decrease before switching to negative residuals later in the water year (Fig. 13B). Between water days 120 and 180, which corresponds to the months of February and March, however, we observe a positive deviation in the trend of decreasing residuals. Average and peak daily rainfall values during this period are not different from preceding months which leads us to conclude that a simple climate mechanism fails to account for this pattern. Instead, because the timing of this positive excursion corresponds with the period of earthflow acceleration noted by Handwerger et al. (2013) using InSAR, we interpret this period of increased sediment concentration to reflect sediment production associated with the delayed (or lagged) acceleration of earthflows. This finding suggests that earthflows may impart a distinct signature in the discharge-concentration relationship of slide-prone systems. Put otherwise, our analysis shows that for a given discharge, sediment concentrations tend to be higher in mid-winter months due to the acceleration of earthflows, imparting a signal that may be reflected in sedimentary records.

3.9. Resistant bedrock and landslide dams

The slow-sliding behavior of landslides in our study area encourages a conceptually appealing and relatively simple rheological modeling framework to interpret and predict long-term controls on landscape form and dynamics in our study area (Booth et al., 2013). During the course of our investigations, however, we discovered landforms indicative of a large, catastrophic

landslide in the Eel River corridor that preclude us from exclusively invoking this perspective to decipher the evolution of the Northern California Coastal Ranges. Motivated by lidar-enabled observations of terrace-like features located at the same elevation along the mainstem of the Eel River, Mackey et al. (2011) documented evidence for a landslide-dammed paleo-lake that dates to 22.5 ky BP. In contrast to the earthflow style of landsliding that has been our focus thus far, the lake-forming landslide appears to have originated from a high-relief, resistant greenstone outcrop. The landslide would have formed a 130 m high dam in order to account for the observed paleo-shoreline features that were originally (and incorrectly) surmised to be fluvial in origin. A 100 m deep landslide scar can be readily observed on the flanks of Nefus Peak and the downslope intersection of that hillslope with the Eel River corresponds with the downstream cessation of paleo-shoreline features (Fig. 3). The dam supported a 55-km long lake that temporarily impounded 1.3 km^3 of water and facilitated delta formation and lacustrine deposition at scattered locations along the Eel River corridor. This previously unrecognized event described by Mackey et al. (2011) correlates with a period of genetic divergence for local anadromous trout (*Oncorhynchus mykiss*) that can be explained by a period of interbreeding downstream of the dam between typically isolated summer- and winter-run ecotypes (Nielsen and Fountain, 1999). Following dam breaching that likely occurred 600 to 6,000 years after dam formation, the steelhead trout reproductive ecotypes reoccupied their preferred geographically isolated spawning areas. The signal of genetic introgression was recognized by Nielsen and Fountain (1999) who attributed the timing of genetic divergence to drought and low-flow conditions, rather than a landslide dam. In addition, the paleo-lake may explain a curious cessation of sediment delivery from the Eel River system that VanLaningham et al. (2008) observed in sediment cores along the continental slope. While much of the landslide dam and paleo-lake evidence has been subsequently erased by pervasive earthflows in the Eel River canyon, the work of Mackey et al. (2011) shows that catastrophic events with long-lived effects contribute to the evolution of the region in diverse and profound ways.

In contrast to the persistent and pervasive activity of earthflows in the Northern California Coastal Ranges, resistant blocks of the Franciscan Complex may fail in a punctuated fashion with widespread impacts. Field observations and lidar imagery indicates that highly sheared and weak matrix enables earthflows to deform or ('flow') around resistant blocks enabling the blocks to become progressively exposed and increasingly prone to bedrock failure. This conceptual model invites an investigation of block size and position in our study area. In this new analysis, we seek to better understand the frequency with which resistant blocks of

sufficient size to dam rivers will be exhumed in our study area. In the Franciscan Complex, resistant bedrock blocks of sandstone, greenstone, chert, and limestone, tend to be elliptical to spheroidal and are often organized in linear 'trains' that parallel structural boundaries, which tend to be northwest-oriented in Northern California (Medley and Lindquist, 1995). A statistical analysis of Franciscan Complex blocks using measurements from field maps and digitized photos demonstrates that block size (estimated as the longest exposed axis) is power-law distributed, implying scale-independence over 7 orders of magnitude (Medley and Lindquist, 1995). We can use this power law distribution to estimate the relative frequency of blocks of a given size in our study area. For example, in our lidar coverage of 226 km^2, this power law distribution implies that blocks with a maximum length of 3 km account for less than 10% of all blocks in the study area. Additionally, 9 km long blocks are likely to comprise less than 2% of the block population. By comparison, the area of the resistant outcrop that anchors Nefus Peak and spawned the Eel-damming landslide 22.5 ky BP has a maximum length of approximately 4 km and is one of the largest resistant blocks observed in our lidar coverage. Furthermore, the density of large (>1 km) blocks observed in our study area is similar to expectations from the Medley and Lindquist (1995) analysis (Fig. 4).

Landslide scaling relationships have been expanded to three dimensions (e.g., Larsen and Montgomery, 2010) enabling us to determine the frequency of landslides with sufficient volume to block the Eel River. Because tributary streams tend to be narrower and steeper, landslide volumes required to induce blockage are much smaller. As a result, the statistical distribution of stream (and valley) size also must also be considered when assessing the potential for landslide damming events. Most simply, the frequency of river-damming events in mélange-dominated mountainous landscapes is dictated by the pace of earthflow activity that exhumes coherent blocks and the convolution of two systems that tend to exhibit power-law scaling: river networks and resistant block sizes. The spatial coincidence of large blocks and high drainage area river valleys increases the likelihood of damming events that can affect large fractions of watersheds similar to what occurred in the Eel River 22.5 ky BP.

4. Summary and synthesis

Our analyses, combined with previously published work, demonstrate that earthflow-prone mountainous landscapes do not behave like idealized sandpiles (i.e., they do not instantaneously and uniformly shed material into valleys in response to channel incision). On the other hand, landslides in our study area are not chaotic or random occurrences. Instead,

landsliding in the Northern California Coastal Ranges is highly localized, yet somehow organized or tuned such that at a given time active slides occupy only a small fraction of the landscape area yet transmit the majority of sediments required to keep pace with rock uplift and baselevel lowering. This observation is all the more remarkable given that the slope angles of active landslides cannot be readily distinguished from the slope angles of relict earthflow terrain, which constitutes the vast majority of our study area (Fig. 14). Our analyses indicate that active landslides erode at an unsustainable pace (e.g., approximately an order of magnitude faster than the background rate of denudation). As a result, zones of active sliding must migrate across the landscape over time in order to maintain the balance between rock uplift and denudation and maintain the relatively uniform distribution of slope angles. We estimate that the recurrence interval of sliding at a given location is on the order of 20kyr, which appears sufficient to maintain roughly uniform slope angles across both inactive and active terrain.

The mechanism that sets the frequency of slope failure at a given location is still unclear. After earthflow activity has denuded a hillslope segment, perhaps weathering must ensue for a period of time in order for weak material to accumulate thickness and flow. Recent analyses indicate that weathering of similar substrate is driven by the position and dynamics of the water table (Rempe and Dietrich, 2014). Material testing of mélange bedrock is notoriously difficult and as a result it is unclear whether significant material alteration and/or weathering beyond wet/dry cycles is required in order for earthflows to initiate. If weathering and hillslope hydrology is a primary factor modulating the evolution of individual earthflows, then our calculations indicate that these processes condition the subsurface for slope instability on timescales of 10^3 to 10^4 yr. More generally, these observations encourage us to revisit the threshold slope model by combining the landslide inventories and kinematic information we describe here with process-based predictions of landslide dynamics and bedrock weathering. The goal of this endeavor would be to predict how changes in rock uplift and incision or climate would alter the frequency and pattern of active landslides.

Because channel processes trim away earthflow toes that impinge on valley floors as well as drive hillslope steepening through vertical incision, the coupling between hillslopes and valleys may also be a key factor dictating zones of slide activity. For example, active landslides are common along the steep, lower reaches of Kekawaka Creek, a tributary to the Eel River. Erosion rate estimates from cosmogenic radionuclides above and below the knickpoint zone on Kekawaka Creek differ by more than a factor of two and average hillslope gradients are steeper

in the lower reaches consistent with predictions from a physically-based earthflow-driven hillslope evolution model. According to our maps, earthflows also exhibit a remarkable tendency to retrogress upslope to ridgelines, liberating accumulated colluvial material that moves downslope and becomes part of the earthflow body. Thus, in addition to baselevel forcing via channel processes, earthflows are also subject to an upslope material supply limitation that regulates their dynamics.

Once active, landslides in our study area tend to exist in a state of chronic failure. Historically, active earthflows in our study area are relatively immune to catastrophic failure, potentially due to hydrologic-mechanical feedbacks, such as dilatant shear strengthening (Iverson, 2005; Schulz et al., 2009a). Furthermore, continued deformation of these slides may enable them to generate their own hydrologic boundaries through the localization of low permeability materials in shear zones and thus become hydrologically isolated (Baum and Reid, 2000). On seasonal timescales, earthflows of varying size exhibit remarkably similar seasonal acceleration and deceleration patterns that lag the onset of seasonal rainfall by months. This seasonal pattern also manifests in suspended sediment records such that earthflows promote higher sediment concentrations months during mid-winter periods.

The highly sheared earthflow-prone materials that constitute much of the Northern California Coastal Ranges are locally interrupted by highly resistant blocks of sandstone, greenstone, or other lithology. Because earthflows can deform around these blocks, the relief of individual blocks appears to increase through time and progressively reveal discontinuities that promote catastrophic bedrock failures. These events are much less frequent than persistent earthflow activity but may have a profound role in shaping valleys as well as perturbing biotic and depositional patterns. These contrasting styles of slope failure highlight the central role of lithology and geologic history in dictating landform evolution and natural hazards.

5. Future directions and opportunities

Landscapes respond to tectonic perturbations through the evolution of channel networks and hillslope form. Given steady state conditions whereby erosion balances rock uplift, uplift causes channels to steepen, leading to increased fluvial incision, baselevel lowering, and increased slope angles. In this sense, changes in topography and stress fields should manifest as changes in total landslide flux, which can be quantified by examining the frequency, magnitude, and velocity of landsliding across wide swaths. Quantitative scaling relationships derived from

the frequency and magnitude of landsliding typically show a power-law decrease in frequency as slide magnitude increases (Hovius et al., 1997; Pelletier et al., 1997; Guzzetti et al., 2002; Malamud et al., 2004; Larsen et al., 2010; Mackey and Roering, 2011; Bennett et al., 2012). This behavior is common regardless of landslide style and triggering mechanisms.

The Eel River catchment provides an opportunity to investigate the relationship between landsliding and tectonic forcing (via baselevel lowering through channel incision). The northwest-southeast trending Central Belt of the Franciscan mélange maintains a constant lithologic and climatic regime that coincides with what has been hypothesized as double-humped zone of uplift (Lock et al., 2006). It is well established that changes in uplift have occurred through time due to the northward migration of the MTJ, yet there are no direct measurements of uplift inland of the coast. Thus, we are currently unable to determine how landsliding patterns change as a result of variable tectonic forcing. We hypothesize that areas with greater uplift rates have larger, faster, and/or more frequent earthflows.

Currently, we have little ability to predict where imminent zones of earthflow activity are likely to arise given that slope angles do not readily distinguish active and inactive earthflows. While most earthflows in our study area span from ridge to channel, a handful occupy midslope positions and it's not obvious whether these features are in the process of elongating or contracting. Historically, the earthflows documented by Mackey and Roering (2011) do not appear to appreciably change their planform extent, so the evolution of earthflow areas may take place slowly or in fits and starts that are infrequently witnessed through monitoring efforts (Baum et al. 1993; Aryal et al., 2012). The rapid vertical lowering of landslide surfaces, sometimes referred to as deflation, however, may provide a key tool for discerning features that have recently experienced a phase of activity and are thus unlikely to experience activity until adjacent slopes become active. This conceptual framework assumes that earthflows are driven by the downslope movement of mobile material in midslope and upslope locations. Mackey et al. (2009) used meteoric [10]Be data to implicate sediment (or colluvium) supply as a potential factor leading to the long-term slowing of an earthflow in our study area. The 2-D numerical modeling results of Booth et al. (2013) demonstrate that a supply-driven landsliding transport law can generate landform patterns and landslide dynamics reminiscent of natural landscapes, although few settings offer observations to thoroughly test these model predictions. The expanding array of geochemical tracers may enable us to better constrain the status and history of active and inactive hillslopes.

Ephemeral meter-scale gully networks are ubiquitous in earthflow-prone landscapes, leaving a distinctive topographic signature. For example, in the Eel River watershed, McLaughlin et al. (2000) used the "rounded, poorly incised, lumpy and irregular topography" resulting from gullied earthflow surfaces in part to identify areas underlain by mélange. We further quantified this topographic signature using slope–area statistics, and found that in the Eel river LiDAR data set, gullies have relatively constant channel slopes of ~25% over drainage areas ranging from ~3000 to 10^6 m^2 (Booth et al., 2013). Areas of high gully density identified with this drainage area criterion correspond to active and dormant earthflow surfaces, while areas of low gully density correspond to stable hillslopes and more widely spaced and well defined channels (Fig. 10). We hypothesize that earthflow deformation continually perturbs the channel network, favoring gullies over the establishment of well-ordered and widely spaced ridge-valley topography common in stable terrain. Furthermore, since currently active earthflows are difficult to distinguish from recently active (but currently dormant) earthflows (Mackey and Roering, 2011), this suggests that characterizing the spatial pattern and extent of gullying with remotely-sensed data might inform investigations of earthflow activity.

The presence of gully networks on active and dormant earthflows also provides an efficient means of delivering sediment to channels adjacent to earthflow toes. Kelsey (1978) found that earthflow movement and surface erosion by gullying contributed approximately equal amounts of sediment to the adjacent channel. Our modeling efforts confirm that gully erosion supplies a some fraction of the material removed from hillslopes in the Eel watershed (Booth and Roering, 2011), and we find that this mechanism is effective even when the toe of an earthflow shows little movement while gullies allows sediments from faster moving upslope sections of the earthflow to bypass slow moving sections and deliver directly to the channel network (Roering et al., 2009). Field-based estimates of sediment delivery by gullies and related earthflow processes are lacking in order to establish their role in sediment production.

The presence of resistant blocks in the Eel River and other landscapes with highly contrasting lithologic properties provides a means for individual outcrops and events to impart a long-lived impact on landscapes by damming rivers, retarding fluvial incision, or suppressing earthflow activity in areas where block densities are high. In each of these scenarios, the influence of resistant bedrock depends on the weathering rate or in-situ comminution rate of the blocks. Our field observations suggest that megaclasts along Kekawaka Creek, for example, are seldom

32

mobilized and do not exhibit evidence for significant weathering. Although we currently lack exposure age data to determine the age of these large boulder-derived knickpoints, it is not unreasonable that they reside in the fluvial system for timescales approaching 10^6 years or longer.

Acknowledgments

References

Agliardi, F., Crosta, G.B., Frattini, P., Malusà, M.G., 2013. Giant non-catastrophic landslides and the long-term exhumation of the European Alps. Earth and Planetary Science Letters, 365, 263-274.

Ahnert, F. 1970. Functional relationships between denudation, relief, and uplift in large, mid-latitude drainage basins. American Journal of Science, 268(3), 243-263.

Andrews, D. J., & Bucknam, R. C., 1987. Fitting degradation of shoreline scarps by a nonlinear diffusion model. Journal of Geophysical Research, 92(B12), 12857-12.

Aryal, A., B. A. Brooks, M. E. Reid, G. W. Bawden, and G. Pawlak, 2012. Displacement Fields from Point Cloud Data: Application of Particle Imaging Velocimetry to Landslide Geodesy, Journal of Geophysical Research - Earth Surface, doi:10.1029/2011JF002161.

Ayoub, F., Leprince, S., Avouac, J.P. 2009, Co-registration and correlation of aerial photographs for ground deformation measurements, ISPRS Journal of Photogrammetry and Remote Sensing, 64, 551-560.

Bak, P., Tang, C., & Wiesenfeld, K., 1987. Self-organized criticality: An explanation of 1/f noise.Physical Review Letters, 59(4), 381-384.

Bak, P., Tang, C., & Wiesenfeld, K., 1988. Self-organized criticality. Physical review A, 38(1), 364-374.

Balco, G., Stone, J. O., Lifton, N. A., & Dunai, T. J., 2008. A complete and easily accessible means of calculating surface exposure ages or erosion rates from ^{10}Be and ^{26}Al measurements. Quaternary Geochronology, 3(3), 174-195.

Balco, G., Finnegan, N.J., Gendaszek, A., Stone, J.O.H., Thompson, N., 2013. Erosional response to northward-propagating crustal thickening in the coastal ranges of the U.S. Pacific Northwest. Am. J. Sci., http://dx.doi.org/ 10.2475/11.2013.01.

Batt, G. E., Cashman, S. M., Garver, J. I., & Bigelow, J. J., 2010. Thermotectonic evidence for two-stage extension on the Trinity detachment surface, Eastern Klamath Mountains, California. American Journal of Science, 310, 261-281.

Baum, R.L., Fleming, R.W., Johnson, A.M., 1993. Kinematics of the Aspen Grove Landslide, Ephraim Canyon, Central Utah, Chapter F of Landslide Processes in Utah – Observations and Theory, US Geological Survey Bulletin 1842. Reston, VA; F1–F34.

Baum, R.L., and M.E. Reid, 2000. Ground water isolation by low-permeability clays in landslide shear zones, (eds.) E. Bromhead, N. Dixon, M. Ibsen, Landslides in Research, Theory and

Practice. Proceedings of the 8th International Symposium on Landslides, vol. 1, Cardiff, Wales, Telford, London, pp. 139–144

Bennett, G. L., Molnar, P., Eisenbeiss, H., & McArdell, B. W., 2012. Erosional power in the Swiss Alps: characterization of slope failure in the Illgraben. Earth Surface Processes and Landforms, 37(15), 1627-1640.

Berti, M., Simoni, A., 2010. Field evidence of pore pressure diffusion in clayey soils prone to landsliding. J. Geophys. Res,, doi:10.1029/2009JF001463

Berti, M., Simoni, A., 2012. Observation and analysis of near-surface pore-pressure measurements in clay-shales slopes. Hydrol. Process. 26 (14), 2187–2205.

Binnie, S. A., Phillips, W. M., Summerfield, M. A., & Fifield, L. K, 2007. Tectonic uplift, threshold hillslopes, and denudation rates in a developing mountain range. Geology, 35(8), 743-746.

Booth, A.M., Roering, J.J., 2011. A 1-D mechanistic model for the evolution of earthflow-prone hillslopes. Journal of Geophysical Research, doi: 10.1029/2011JF002024.

Booth, A.M., Roering, J.J., Rempel, A.W., 2013. Topographic signatures of deep-seated landslides and a general landscape evolution model. J. Geophys. Res. Earth Surf, http://dx.doi.org/10.1002/jgrf.20051.

Booth, A. M., Lamb, M. P., Avouac, J. P., & Delacourt, C., 2013. Landslide velocity, thickness, and rheology from remote sensing: La Clapière landslide, France. Geophysical Research Letters, 40(16), 4299-4304.

Borgomeo, E., Hebditch, K. V., Whittaker, A. C., & Lonergan, L., 2014. Characterising the spatial distribution, frequency and geomorphic controls on landslide occurrence, Molise, Italy. Geomorphology, doi:10.1016/j.geomorph.2014.08.004.

Bovis, M.J., Jones, P., 1992. Holocene history of earthflow mass movements in south- central British Columbia-The influence of hydroclimatic changes. Can. J. Earth Sci. 29, 1746–1755.

Brown, W. M., Ritter, J. R., 1971. Sediment transport and turbidity in the Eel River basin, California, USGS Water Supply Paper 1986, 69p.

Brückl, E., Brunner, F. K., & Kraus, K., 2006. Kinematics of a deep‐seated landslide derived from photogrammetric, GPS and geophysical data. Engineering Geology, 88(3), 149-159.

Brunetti, M. T., Guzzetti, F., & Rossi, M., 2009. Probability distributions of landslide volumes. Nonlinear Processes in Geophysics, 16(2), 179-188.

Brunsden, D., 1993. Mass movement; the research frontier and beyond: a geomorphological approach. Geomorphology, *7*(1), 85-128.

Brunsden, D., 1999. Some geomorphological considerations for the future development of landslide models. Geomorphology, 30(1), 13-24.

Burbank, D. W., Leland, J., Fielding, E., Anderson, R. S., Brozovic, N., Reid, M. R., & Duncan, C., 1996. Bedrock incision, rock uplift and threshold hillslopes in the northwestern Himalayas. Nature, 379(6565), 505-510.

Bürgmann, R., Rosen, P. A., & Fielding, E. J., 2000. Synthetic aperture radar interferometry to measure Earth's surface topography and its deformation. Annual Review of Earth and Planetary Sciences, 28(1), 169-209.

Bürgmann, R., and W. Thatcher, 2013. Space geodesy: a revolution in crustal deformation measurements of tectonic processes, in: The Web of Geological Sciences: Advances, Impacts, and Interactions, edited by M. E. Bickford, Geological Society of America Special Paper 500, doi:10.1130/2013.2500(12).

Calabro, M.D., Schmidt, D.A., Roering, J.J., 2010. An examination of seasonal deformation at the Portuguese Bend landslide, southern California, using radar interferometry, Journal of Geophysical Research, doi:/10.1029/2009JF001314.

California Department of Water Resources, 1965, North Coastal Area Investigation, Bulletin No. 136, Department of Water Resources.

California Department of Water Resources, 1970, Middle Fork Landslide Investigation: Technical Report, Department of Water Resources.

Carson, M. A., & Petley, D. J.,1970. The existence of threshold hillslopes in the denudation of the landscape. Transactions of the Institute of British Geographers, 49, 71-95.

Casson, B., Delacourt, C., Allemand, P., 2005. Contribution of multi-temporal remote sensing images to characterize landslide slip surface? Application to the La Clapière landslide (France). Natural Hazards and Earth System Science, 5(3), 425-437.

Cendrero, A., & Dramis, F., 1996. The contribution of landslides to landscape evolution in Europe. Geomorphology, 15(3), 191-211.

Cerovski-Darriau, C., J.J. Roering, M. Marden, A.S. Palmer, and E.L. Bilderback, 2014. Quantifying temporal variations in landslide-driven sediment production by reconstructing paleolandscapes using tephrochronology and lidar: Waipaoa River, New Zealand, G-cubed (Geochemistry, Geophysics, and Geosystems), doi: 10.1002/2014GC005467.

Clarke, B.A., Burbank, D.W., 2010. Evaluating hillslope diffusion and terrace riser degradation in New Zealand and Idaho. Journal of Geophysical Research: Earth Surface, 115(F2).

Coe, J.A., Ellis, W.L., Godt, J.W., Savage, W.Z., Savage, J.E., Michael, J.A., Kibler, J.D., Powers, P.S., Lidke, D.J., Debray, S., 2003. Seasonal movement of the Slumgullion landslide determined from global positioning system surveys and field instrumentation, July 1998–March 2002. Engineering Geology, 68, 67–101.

Coe, J. A., McKenna, J. P., Godt, J. W., Baum, R. L., 2009. Basal‑topographic control of stationary ponds on a continuously moving landslide, Earth Surface Processes and Landforms, 34(2), 264-279.

Cohen, S., Kettner, A. J., & Syvitski, J. P., 2014. Global suspended sediment and water discharge dynamics between 1960 and 2010: Continental trends and intra-basin sensitivity. Global and Planetary Change, 115, 44-58.

Costa, J. E., & Schuster, R. L., 1988. The formation and failure of natural dams. Geological Society of America Bulletin, 100(7), 1054-1068.

Daehne, A., & Corsini, A., 2012. Kinematics of active earthflows revealed by digital image correlation and DEM subtraction techniques applied to multi‑temporal LiDAR data. Earth Surface Processes and Landforms, 38, 640-654.

de la Noe, G., de Margerie, E., 1888. Les Formes du Terrain. Service Geographique de l'Armee. Imprimerie Nationale, Paris, 205 pp.

DeLong, S. B., Prentice, C. S., Hilley, G. E., Ebert, Y., 2012. Multitemporal ALSM change detection, sediment delivery, and process mapping at an active earthflow. Earth Surface Processes and Landforms, 37(3), 262-272.

Densmore, A.L., Anderson, R.S., McAdoo, B.G., Ellis, M.A., 1997. Hillslope evolution by bedrock landslides. Science, 275(5298), 369-372.

Densmore, A.L., Hovius, N., 2000. Topographic fingerprints of bedrock landslides. Geology, v. 28, 371–374.

Di Maio, C., Vassallo, R., Vallario, M., Calcaterra, S., & Gambino, P., 2013. Surface and deep displacements evaluated by GPS and inclinometers in a clayey slope. In Landslide Science and Practice (pp. 265-271). Springer Berlin Heidelberg.

DiBiase, R. A., Whipple, K. X., Heimsath, A. M., & Ouimet, W. B, 2010. Landscape form and millennial erosion rates in the San Gabriel Mountains, CA. Earth and Planetary Science Letters, 289(1), 134-144.

Dumitru, T. A., 1991. Major Quaternary uplift along the northernmost San Andreas fault, King Range, northwestern California. Geology, 19(5), 526-529.

Dwyer, M.J., Scott, R.G., Lorens, P.J., 1971. Landslide Conditions and Related Sediment Production on the Eel River: Red Bluff, California, California Department of Water Resources, Northern District, 69 p.

Egholm, D. L., Knudsen, M. F., & Sandiford, M., 2013. Lifespan of mountain ranges scaled by feedbacks between landsliding and erosion by rivers. Nature, 498(7455), 475-478.

Ekström, G., & Stark, C. P., 2013. Simple scaling of catastrophic landslide dynamics. Science, 339 (6126), 1416-1419.

Ferrier, K. L., Kirchner, J. W., & Finkel, R. C., 2005. Erosion rates over millennial and decadal timescales at Caspar Creek and Redwood Creek, northern California Coast Ranges. Earth Surface Processes and Landforms, 30, 1025-1038.

Fuller, T. K., Perg, L. A., Willenbring, J. K., Lepper, K., 2009. Field evidence for climate-driven changes in sediment supply leading to strath terrace formation. Geology, 37(5), 467-470.

Furlong, K.P., Govers, R., 1999. Ephemeral crustal thickening at a triple junction: The Mendocino crustal conveyor. Geology 27 (20), 127–130.

Furlong, K.P., Schwartz, S.Y., 2004. Influence of the Mendocino triple junction on the tectonics of coastal California, Annual Review of Earth and Planetary Sciences, 32, 403-433.

García-Davalillo, J. C., Herrera, G., Notti, D., Strozzi, T., & Álvarez-Fernández, I., 2013. DInSAR analysis of ALOS PALSAR images for the assessment of very slow landslides: the Tena Valley case study. Landslides, 11, 1-22.

Gelhar, L. W., Welty, C., & Rehfeldt, K. R., 1992. A critical review of data on field‐scale dispersion in aquifers. Water resources research, 28(7), 1955-1974.

Giordan, D., Allasia, P., Manconi, A., Baldo, M., Santangelo, M., Cardinali, M., Corazza, A., Albanese, V., Lollino, G., Guzzetti, F. 2013. Morphological and kinematic evolution of a large earthflow: The Montaguto landslide, southern Italy. Geomorphology 187, 61-79.

Glen, J. W., 1955. The creep of polycrystalline ice, P. Roy. Soc. Lond. A Mat., 228, 519–538.

Granger, D. E., Kirchner, J. W., & Finkel, R., 1996. Spatially averaged long-term erosion rates measured from in situ-produced cosmogenic nuclides in alluvial sediment. The Journal of Geology, 104, 249-257.

Granger, D. E., Lifton, N. A., & Willenbring, J. K., 2013. A cosmic trip: 25 years of cosmogenic nuclides in geology. Geological Society of America Bulletin, doi:10.1130/B30774.1.

Guerriero, L., Coe, J. A., Revellino, P., Grelle, G., Pinto, F., & Guadagno, F. M., 2014, Influence of slip-surface geometry on earth-flow deformation, Montaguto earth flow, southern Italy. Geomorphology, doi:10.1016/j.geomorph.2014.04.039

Guzzetti, F., Malamud, B. D., Turcotte, D. L., & Reichenbach, P., 2002. Power-law correlations of landslide areas in central Italy. Earth and Planetary Science Letters, 195(3), 169-183.

Guzzetti, F., Mondini, A.C., Cardinali, M., Fiorucci, F., Santangelo, M., Chang, K.T., 2012. Landslide inventory maps: New tools for an old problem. Earth-Science Reviews 112(1), 42-66.

Handwerger, A.L., Roering, J.J., Schmidt, D.A., 2013. Controls on the seasonal deformation of slow-moving landslides. Earth. Plan. Sci. Lett., doi:10.1016/j.epsl.2013.06.047

Handwerger, A.L.*, J.J. Roering, D.A. Schmidt, and A.W. Rempel, (in review), Kinematics of earthflows in the Northern California Coast Ranges using satellite interferometry, Geomorphology.

Haneberg, W.C., 1991. Pore pressure diffusion and the hydrologic response of nearly saturated, thin landslide deposits to rainfall. Journal of Geology. 99, 886–892.

Harden, D.R., Colman, S.M., Nolan, K.M., 1995. Mass movement in the Redwood Creek basin, northwestern California: in Nolan, K. M., et al., eds., Geomorphic processes and aquatic habitat in the Redwood Creek basin, northwestern California: U.S. Geological Survey Professional Paper 1454, pp. G1-G11.

Harp, E. L., Keefer, D. K., Sato, H. P., & Yagi, H., 2011. Landslide inventories: the essential part of seismic landslide hazard analyses. Engineering Geology, 122(1), 9-21.

Hicks, D.M., Gomez, B., Trustrum, N.A., 2000. Erosion thresholds and suspended sediment yields, Waipaoa River Basin, New Zealand. Water Resources Research, 36, 1129–1142.

Hilley, G.E., Bürgmann, R., Ferretti, A., Novali, F., Rocca, F., 2004. Dynamics of slow- moving landslides from permanent scatterer analysis. Science 304, 1952–1955.

Hollingsworth, J., S. Leprince, F. Ayoub, J.P., Avouac, 2012. Deformation during the 1975-1984 Krafla rifting crisis, NE Iceland, measured from historical optical imagery, J. Geophys. Res., doi:1001029/2012JB009140.

Hovius, N., Stark, C.P., Allen, P.A., 1997. Sediment flux from a mountain belt derived by landslide mapping, Geology, 25(3), 231-234.

Hovius, N., Stark, C. P., Hao‑Tsu, C., & Jiun‑Chuan, L., 2000. Supply and removal of sediment in a landslide‑dominated mountain belt: Central Range, Taiwan. The Journal of Geology, 108(1), 73-89.

Huang, M. Y. F., & Montgomery, D. R., 2012. Fluvial response to rapid episodic erosion by earthquake and typhoons, Tachia River, central Taiwan. Geomorphology, 175, 126-138.

Iverson, R. M., 1986a. Dynamics of slow landslides: A theory for time dependent behavior, in Hillslope Processes, edited by A. D. Abrahams, pp. 297–317, Allen and Unwin, Winchester, MA.

Iverson, R. M., 1986b. Unsteady, nonuniform landslide motion: 1. Theoretical dynamics and the steady datum state, J. Geol., 94, 1–15.

Iverson, R.M., 1986c. Unsteady, nonuniform landslide motion: 2. Linearized theory and the kinematics of transient response, J. Geol., 94, 349–364.

Iverson, R.M., 2000. Landslide triggering by rain infiltration. Water Resour. Res. 36, 1897–1910

Iverson, R.M., 2005. Regulation of landslide motion by dilatancy and pore-pressure feedback. J. Geophys. Res., doi: 10.1029/2004JF000268.

Iverson, R. M., Reid, M. E., Iverson, N. R., LaHusen, R. G., Logan, M., Mann, J. E., & Brien, D. L., 2000. Acute sensitivity of landslide rates to initial soil porosity. Science, 290(5491), 513-516.

Iverson, R.M., Major, J.J., 1987. Rainfall, ground-water flow, and seasonal movement at Minor Creek landslide, northwestern California: Physical interpretation of empirical relations. Geol. Soc. Am. Bull. 99, 579–594, http://dx.doi.org/10.1130/0016-7606.

Jayko, A.S., Blake, M.C., McLaughlin, R.J., Ohlin, H.N., Ellen, S.D., and Kelsey, H.M., 1989. Reconnaissance Geologic Map of the Covelo 30-by 60-Minute Quadrangle, Northern California: U.S. Geological Survey Miscellaneous Field Investigation Map MF-2001, scale 1:100 000.

Katz, O., & Aharonov, E., 2006. Landslides in vibrating sand box: What controls types of slope failure and frequency magnitude relations?. Earth and Planetary Science Letters, 247(3), 280-294.

Keefer, D., Johnson, A., 1983. Earth flows: morphology, mobilization, and movement, USGS Professional Paper 1264.

Keefer, D., 1994. The importance of earthquake-induced landslides to long-term slope erosion and slope-failure hazards in seismically active regions. Geomorphology 10, 265–284.

Keefer, D.K., 2002. Investigating landslides caused by earthquakes–a historical review, Surveys in Geophysics, 23, 473–510.

Kelsey, H.M., 1977. Landsliding, Channel Changes, Sediment Yield and Land Use in the Van Duzen River Basin, North Coastal California, 1941–1975 [Ph.D. thesis]: Santa Cruz, University of California, 370 p.

Kelsey, H.M., 1978. Earthflows in Franciscan mélange, Van Duzen River basin, California. Geology 6, 361–364.

Kelsey, H.M., 1980. A sediment budget and an analysis of geomorphic process in the Van Duzen River Basin, north coastal California, 1941–1975—Summary. Geol. Soc. Am. Bull. 91 (4), 190–195.

Kelsey, H.M., Carver, G.A., 1988. Late Neogene and Quaternary tectonics associated with northward growth of the San Andreas transform fault, northern California. Journal of Geophysical Research: Solid Earth (1978–2012), 93(B5), 4797-4819.

Korup, O., 2008. Rock type leaves topographic signature in landslide-dominated mountain ranges. Geophysical Research Letters, 35(11), L11402, doi: 10.1029/2008GL034157

Korup, O., Clague, J. J., Hermanns, R. L., Hewitt, K., Strom, A. L., & Weidinger, J. T., 2007. Giant landslides, topography, and erosion. Earth and Planetary Science Letters, 261(3), 578-589.

Korup, O., Densmore, A. L., & Schlunegger, F., 2010, The role of landslides in mountain range evolution. Geomorphology, 120(1), 77-90.

Korup, O., Görüm, T., Hayakawa, Y, 2012. Without power? Landslide inventories in the face of climate change. Earth Surface Processes and Landforms, 37(1), 92-99.

Larsen, I.J., Montgomery, D.M., Korup, O., 2010. Landslide erosion controlled by hillslope material. Nature Geoscience 3, 247–251.

Larsen, I.J., Montgomery, D.M., 2012. Landslide erosion coupled to tectonics and river incision. Nature Geoscience 5, 468-473.

Larsen, I. J., Montgomery, D. R., & Greenberg, H. M., 2014. The contribution of mountains to global denudation. Geology, 42(6), 527-530.

Leprince, S., Berthier, E., Ayoub, F., Delacourt, C., & Avouac, J. P., 2008. Monitoring Earth surface dynamics with optical imagery. Eos, Transactions American Geophysical Union, 89(1), 1-2.

Li, G., West, A.J., Densmore, A., Jin, Z.D., Parker, R., and Hilton, R.G. 2014. Seismic mountain building: landslides associated with the 2008 Wenchuan earthquake in the context of a

generalized model for earthquake volume balance. Geochemistry, Geophysics, Geosystems 15: 833-844.

Lock, J., Kelsey, H., Furlong, K., Woolace, A., 2006. Late Neogene and quaternary landscape evolution of the northern California Coast Ranges: Evidence for Mendocino triple junction tectonics. Geol. Soc. Am. Bull. 118, 1232–1246.

Lopes, V. L., & Ffolliott, P. F., 1993. Sediment rating curves for a clearcut Ponderosa Pine watershed in Northern Arizona, Journal of the American Water Resources Association, 29(3), 369-382.

Mackey, B.H., Roering, J.J., 2011. Sediment yield, spatial characteristics, and the long- term evolution of active earthflows determined from airborne LiDAR and historical aerial photographs, Eel River, California. Geol. Soc. Am. Bull. 123, 1560–1576, http://dx.doi.org/10.1130/B30306.1.

Mackey, B.H., Roering, J.J., McKean, J.A., 2009. Long-term kinematics and sediment flux of an active earthflow, Eel River, California. Geology 37, 803–806.

Mackey, B.H., J.J. Roering, M.P. Lamb, 2011. Landslide-dammed paleolake perturbs anadromous fish evolution and marine sedimentation. Proceedings of the National Academy of Science, doi:10.1073/pnas.1110445108, 1-5

Major, J. J., 2004. Posteruption suspended sediment transport at Mount St. Helens: Decadal‐scale relationships with landscape adjustments and river discharges. Journal of Geophysical Research: Earth Surface (2003–2012), doi:10.1029/2002JF000010.

Malamud, B.D., Turcotte, D.L., Guzzetti, F., Reichenbach, P., 2004. Landslide inventories and their statistical properties. Earth Surface Processes and Landforms 29, 687-711.

Malet, J. P., Maquaire, O., & Calais, E., 2002. The use of Global Positioning System techniques for the continuous monitoring of landslides: application to the Super-Sauze earthflow (Alpes-de-Haute-Provence, France). Geomorphology, 43(1), 33-54.

Malhase, J., 1938. Landslide at mile post 201 telegraph poles 9 to 12, Northwestern Pacific Railroad. Memorandum.

McLaughlin, R.J., Kling, S.A., Poore, R.Z., McDougall, K., Beutner, E.C., 1982. Post–Middle Miocene accretion of Franciscan rocks, northwestern California: Geological Society of America Bulletin 93(7), 595–605.

McLaughlin, R.J., Ellen, S.D., Blake Jr., M.C., Jayko, A.S., Irwin, W.P., Aalto, K.R., Carver, G.A., Clarke Jr., S.H., 2000. Geology of the Cape Mendocino, Eureka, Garberville, and southwestern part of the Hayfork 30 × 60 minute quadrangles and adjacent offshore area,

Northern California. U.S. Geological Survey Miscellaneous Field Studies Map MF-2336, 1:100000 scale.

Medley, E., & Lindquist, E. S., 1995. The engineering significance of the scale-independence of some Franciscan melanges in California, USA. In Proceeding of the 35th US Rock Mechanics Symposium. Rotterdam: AA Balkema (pp. 907-914).

Meigs, A., Brozovic, N., & Johnson, M. L., 1999. Steady, balanced rates of uplift and erosion of the Santa Monica Mountains, California. Basin Research, 11(1), 59-73.

Merritts, D., Bull, W. B., 1989. Interpreting Quaternary uplift rates at the Mendocino triple junction, northern California, from uplifted marine terraces. Geology, 17(11), 1020-1024.

Merritts, D. J., 1996. The Mendocino triple junction: Active faults, episodic coastal emergence, and rapid uplift. Journal of Geophysical Research, 101(B3), 6051-6070.

Meunier, P., Hovius, N., Haines, J.A., 2008. Topographic site effects and the location of earthquake induced landslides. Earth and Planetary Science Letters 275, 221–232.

Montgomery, D. R., 2001. Slope distributions, threshold hillslopes, and steady-state topography. American Journal of Science, 301(4-5), 432-454.

Montgomery, D. R., & Brandon, M. T., 2002. Topographic controls on erosion rates in tectonically active mountain ranges. Earth and Planetary Science Letters, 201(3), 481-489.

Muhs, D.R., Thorson, R.M., Clague, J.J., Mathews, W.H., McDowell, P.F., Kelsey, H.M., 1987. Pacific Coast and mountain system, in Graf, W.L., ed., Geomorphic Systems of North America: Boulder, Colorado, Geological Society of America, p. 517–581.

Neuman, S. P., 1990. Universal scaling of hydraulic conductivities and dispersivities in geologic media. Water resources research, 26(8), 1749-1758.

Nichol, J., & Wong, M.S., 2005. Satellite remote sensing for detailed landslide inventories using change detection and image fusion. International Journal of Remote Sensing, 26(9), 1913-1926.

Nielsen, J. L., & Fountain, M. C., 1999. Microsatellite diversity in sympatric reproductive ecotypes of Pacific steelhead (Oncorhynchus mykiss) from the Middle Fork Eel River, California. Ecology of Freshwater Fish, 8(3), 159-168.

Nittrouer, C. A., 1999. STRATAFORM: overview of its design and synthesis of its results. Marine Geology, 154(1), 3-12.

Nolan, K. M., & Janda, R. J., 1995. Movement and sediment yield of two earthflows, northwestern California. USDI Geological Survey Professional Paper, 1454.

Ouimet, W. B., Whipple, K. X., & Granger, D. E, 2009. Beyond threshold hillslopes: Channel adjustment to base-level fall in tectonically active mountain ranges. Geology, 37(7), 579-582.

Palmquist, R. C., & Bible, G., 1980. Conceptual modelling of landslide distribution time and space. Bulletin of the International Association of Engineering Geology, 21(1), 178-186.

Parker, R. N., Densmore, A. L., Rosser, N. J., De Michele, M., Li, Y., Huang, R.,, S. Whadcoat, & Petley, D. N., 2011. Mass wasting triggered by the 2008 Wenchuan earthquake is greater than orogenic growth. Nature Geoscience, 4(7), 449-452.

Pelletier, J. D., Malamud, B. D., Blodgett, T., & Turcotte, D. L., 1997. Scale-invariance of soil moisture variability and its implications for the frequency-size distribution of landslides. Engineering Geology, 48(3), 255-268.

Portenga, E. W., & Bierman, P. R., 2011. Understanding Earth's eroding surface with 10 Be. GSA Today, 21(8), 4-10.

Putnam, W.C., and Sharp, R.P., 1940, Landslides and earthflows near Ventura, southern California: Geographical Review, 30, 591-600.

Reid, M.E., 1994. A pore-pressure diffusion model for estimating landslide-inducing rainfall. J. Geol. 102, 709–717.

Rempe, D. M., & Dietrich, W. E., 2014. A bottom-up control on fresh-bedrock topography under landscapes. Proceedings of the National Academy of Sciences, 111(18), 6576-6581.

Reusser, L. J., & Bierman, P. R., 2010. Using meteoric 10Be to track fluvial sand through the Waipaoa River basin, New Zealand. Geology, 38(1), 47-50.

Roering, J., 2012. Tectonic geomorphology: Landslides limit mountain relief. Nature Geoscience, 5(7), 446-447.

Roering, J. J., Kirchner, J. W., & Dietrich, W. E, 1999, Evidence for nonlinear, diffusive sediment transport on hillslopes and implications for landscape morphology. Water Resources Research, 35(3), 853-870.

Roering, J. J., Kirchner, J. W., Sklar, L. S., & Dietrich, W. E., 2001. Hillslope evolution by nonlinear creep and landsliding: An experimental study. Geology, 29(2), 143-146.

Roering, J. J., Kirchner, J. W., & Dietrich, W. E., 2005. Characterizing structural and lithologic controls on deep-seated landsliding: Implications for topographic relief and landscape evolution in the Oregon Coast Range, USA. Geological Society of America Bulletin, 117(5-6), 654-668.

Roering, J. J., Perron, J. T., & Kirchner, J. W., 2007. Functional relationships between denudation and hillslope form and relief. Earth and Planetary Science Letters, 264(1), 245-258.

Roering, J.J., Stimely, L.L., Mackey, B.H., Schmidt, D.A., 2009. Using DInSAR, airborne LiDAR, and archival air photos to quantify landsliding and sediment transport. Geophys. Res. Lett. 36, L040374, doi: 10.1029/2009GL040374.

Rosen, P. A., Hensley, S., Peltzer, G., & Simons, M., 2004. Updated repeat orbit interferometry package released. Eos, Transactions American Geophysical Union, 85(5), 47-47.

Rutter, E. H., & Green, S., 2011. Quantifying creep behaviour of clay-bearing rocks below the critical stress state for rapid failure: Mam Tor landslide, Derbyshire, England. Journal of the Geological Society, 168(2), 359-372.

Scheingross, J. S., Minchew, B. M., Mackey, B. H., Simons, M., Lamb, M. P., & Hensley, S., 2013. Fault-zone controls on the spatial distribution of slow-moving landslides. Geological Society of America Bulletin, 125(3-4), 473-489.

Schmidt, D. A., & Bürgmann, R., 2003. Time-dependent land uplift and subsidence in the Santa Clara valley, California, from a large interferometric synthetic aperture radar data set. Journal of Geophysical Research, 108(B9), 2416, doi: 10.1029/2002JB002267

Schulz, W. H., McKenna, J. P., Biavati, G. and Kibler, J. D. 2009a. Relations between hydrology and velocity of a continuously moving landslide evidence of pore-pressure feedback regulating landslide motion? Landslides, 6, 181-190.

Schulz, W. H., Kean, J. W., & Wang, G., 2009b, Landslide movement in southwest Colorado triggered by atmospheric tides. Nature Geoscience, 2(12), 863-866.

Schwab, M., Rieke-Zapp, D., Schneider, H., Liniger, M., & Schlunegger, F, 2008. Landsliding and sediment flux in the Central Swiss Alps: a photogrammetric study of the Schimbrig landslide, Entlebuch. Geomorphology, 97, 392-406.

Scott, R.G., 1973. Geology and Sediment Production for Ten Eel River Landslides: Red Bluff, CA, California Department of Water Resources, Northern District, Memorandum Report, 29 p.

Simon, T., 2001. The River Stops Here Saving Round Valley, A Pivotal Chapter in California's Water Wars, UC Press, 400p.

Simoni, A., Ponza, A., Picotti, V., Berti, M., Dinelli, E., 2013. Earthflow sediment production and Holocene sediment record in a large Apennines catchment. Geomorphology 188, 42–53.

Skempton, A. W., Leadbeater, A. D., & Chandler, R. J., 1989. The Mam Tor landslide, North Derbyshire. Philosophical Transactions of the Royal Society of London. Series A, Mathematical and Physical Sciences, 329, 503-547.

Sloan, J., Miller, J. R., & Lancaster, N., 2001. Response and recovery of the Eel River, California, and its tributaries to floods in 1955, 1964, and 1997. Geomorphology, 36(3), 129-154.

Smith, B.J., Tilton, W.C., Elko, J.M., Jacobus, C.D., 1974. Eel River Basin Environmental Studies: Red Bluff, California, California Department of Water Resources, Northern District, 93p.

Sommerfield, C. K., Nittrouer, C. A., 1999. Modern accumulation rates and a sediment budget for the Eel shelf: a flood-dominated depositional environment. Marine Geology, 154(1), 227-241.

Sommerfield, C. K., Drake, D. E., Wheatcroft, R. A., 2002. Shelf record of climatic changes in flood magnitude and frequency, north-coastal California. Geology, 30(5), 395-398.

Sommerfield, C. K., Wheatcroft, R. A., 2007. Late Holocene sediment accumulation on the northern California shelf: Oceanic, fluvial, and anthropogenic influences. Geological Society of America Bulletin, 119(9-10), 1120-1134.

Stark, C. P., & Hovius, N., 2001. The characterization of landslide size distributions. Geophysical Research Letters, 28(6), 1091-1094.

Stark, C.P., & Guzzetti, F., 2009. Landslide rupture and the probability distribution of mobilized debris volumes. Journal of Geophysical Research: Earth Surface, doi: 10.1029/2008JF001008.

Strahler, A. N., 1950. Equilibrium theory of erosional slopes approached by frequency distribution analysis. Part I. American Journal of Science, 248, 673-696.

Syvitski, J. P., Morehead, M. D., Bahr, D. B., & Mulder, T., 2000. Estimating fluvial sediment transport: the rating parameters. Water Resources Research, 36(9), 2747-2760.

Syvitski, J.P., and Morehead, M.D., 1999, Estimating river-sediment discharge to the ocean: application to the Eel margin, northern California: Marine Geology, 154, 13-28.

Tarolli, P., 2014. High-resolution topography for understanding Earth surface processes: Opportunities and challenges. Geomorphology, 216, 295-312.

van Asch, T. W. J., 2005. Modelling the hysteresis in the velocity pattern of slow‐moving earth flows: the role of excess pore pressure. Earth Surface Processes and Landforms, 30(4), 403-411.

van den Eeckhaut, M., Poesen, J., Govers, G., Verstraeten, G., Demoulin, A., 2007. Characteristics of the size distribution of recent and historical landslides in a populated hilly region. Earth and Planetary Science Letters, 256(3), 588-603.

vanLaningham, S., Duncan, R. A., Pisias, N. G., & Graham, D. W., 2008. Tracking fluvial response to climate change in the Pacific Northwest: a combined provenance approach using Ar and Nd isotopic systems on fine-grained sediments. Quaternary Science Reviews, 27(5), 497-517.

Varnes, D. J. & Savage, W. Z. (eds), 1996. The Slumgullion earth flow: A large-scale natural laboratory. US Geolological Survey Bulletin 2130.

Vulliet, L., 2000. Natural slopes in slow movement, in Modeling in Geomechanics, edited by M. Zaman, J. R. Booker, and G. Gioda, pp. 654–676, John Wiley & Sons, Chichester, UK.

Vulliet, L., and K. Hutter, 1988a. Continuum model for natural slopes in slow movement, Geotechnique, 38, 199–217.

Vulliet, L., and K. Hutter, 1988b. Set of constitutive models for soils under slow movement, J. Geotech. Eng.-ASCE, 114, 1022–1041.

Vulliet, L., and K. Hutter, 1988c. Viscous-type sliding laws for landslides, Can. Geotech. J., 25, 467–477.

Wahrhaftig, C., Curry, R. R., 1967. Geologic implications of sediment discharge records from Northern Coast Ranges, California, in Man's effect on California watersheds: Report of the California Assembly Committee on Natural Resources, Planning, and Public Works, Subcommittee on Forestry and Watershed Management, Part III, p. 35-58

Walling, D. E., & Webb, B. W., 1996. Erosion and sediment yield: a global overview. IAHS Publications-Series of Proceedings and Reports-Intern Assoc Hydrological Sciences, 236, 3-20.

Wheatcroft, R.A., Sommerfield, C.K., 2005. River sediment flux and shelf sediment accumulation rates on the Pacific Northwest margin. Cont. Shelf Res. 25, 311–332.

Willenbring, J. K., Gasparini, N. M., Crosby, B. T., & Brocard, G., 2013a. What does a mean mean? The temporal evolution of detrital cosmogenic denudation rates in a transient landscape. Geology, 41(12), 1215-1218.

Willenbring, J. K., Codilean, A. T., & McElroy, B., 2013b. Earth is (mostly) flat: Apportionment of the flux of continental sediment over millennial time scales. Geology, 41(3), 343-346.

Zhang, X., Phillips, C., Marden, M., 1993. A comparison of earthflow movement mechanisms on forested and grassed slopes, Raukumara Peninsula, North Island, New Zealand. Geomorphology, 6, 175-187.

Zhao, C., Lu, Z., Zhang, Q., de la Fuente, J., 2012. Large-area landslide detection and monitoring with ALOS/PALSAR imagery data over Northern California and Southern Oregon, USA. Remote Sens. Environ. 124, 348–359.

Figure captions

Fig. 1. Expected earthflow morphology and natural hillslopes. A) Schematic earthflow showing primary morphologic and kinematic zones. Modified from Keefer and Johnson (1983) and USGS. B) Airborne lidar shaded relief image of hillslope near the Eel River and Boulder Creek confluence showing a mosaic of active and inactive earthflows and gullies. Note the abundance of relict amphitheater-shaped accumulation zones along the ridgeline.

Fig. 2. Relief image of study area in Northern California showing the Mendocino Triple Junction and associated plate boundaries as well as the outline of the landslide-prone Franciscan Complex. The area of lidar coverage used for the air photo landslide inventory is shown in red. Modified from Google Earth image.

Fig. 3. Photographic perspectives from Northern California study area. A) View upstream along the Eel River corridor near the confluence of Kekawaka Creek and the Eel River. Note the consistent and relatively low-gradient hillslopes. B) Eel River tributary view looking upstream just above a boulder-dominated knickpoint. Note the wide aggradational surface. The blue vertical line is 1.8 meter person for scale. C) Same location as in B, but looking downstream across the mega-boulder knickpoint. Note the active earthflow toe on river left with 20 m scale. D) Three-dimensional digital reconstruction of 22.5 ky BP paleolake formed by a catastrophic landslide dam emanating from a resistant block (modified from Mackey et al., 2011). View is upstream (looking south-southeast) and from just above Nefus Peak. The Kekawaka/Eel confluence is on the left in the foreground.

Fig. 4. Perspective view of shaded relief lidar data looking east into the Kekawaka Creek tributary with the Eel River confluence in the foreground. In the foreground, an 8-km stretch of the Eel River flows from right to left. Resistant bedrock blocks (e.g., meta-sandstone, blueschist, and meta-basalt) form high-relief areas (red) which contrast with low-gradient terrain composed of argillaceous mudstone and mélange that is shaped by active earthflows (yellow) that flow around the resistant blocks.

Fig. 5. Shaded relief map (10 m DEM) of the Eel River field area covered by InSAR (modified from Handwerger et al., in review). Red polygons show active landslides identified and mapped using InSAR. Green polygons show landslides previously mapped using airborne lidar and historical imagery in the zone of lidar coverage (Mackey and Roering, 2011). Black polygons show slides mapped with lidar and historical photos. See Fig. 8 for more detail in the region with lidar data. The light blue filled area outlines the Central and Eastern belts of the Franciscan Complex. Inset in the upper right corner shows relative location within California.

Fig. 6. Example of historical landslide velocity estimation using A) historical imagery in 1944 and B) airborne lidar shaded relief image in 2006 with vegetation colored in green to track the location of markers (trees and shrubs) that translate atop an active earthflow. C) Composite image of lidar and historical image with red vectors showing 62-years of displacement. The thin

black line denotes active earthflow boundaries based on morphology characteristic of earthflows and displaced markers.

Fig. 7. Earthflow mapping derived from historical air photos. A) Map of lidar coverage and active earthflows modified from Mackey and Roering (2011). B–D) Selection of active earthflows. Note the variance in planform shape that contrasts with the conceptual model shown in Fig. 1. Most active earthflows connect to the channel network and several span channel to ridgeline. Contour interval is 200 m. Coordinates are UTM zone 10 N.

Fig. 8. Map of SAR interferogram stack draped over lidar hillshade, Eel River. Colorscale represents average deformation over a 4 year period (modified from Handwerger et al., in review). Negative values correspond to motion towards the satellite. Green polygons show earthflows mapped by Mackey and Roering (2011). Short black lines show tree vector displacement between 1944-2006 (Mackey and Roering, 2011). The LOS (line of sight) vector shows the trajectory (N–NW) and look direction (E–NE) of the PALSAR satellite.

Fig. 9. Map of movement of the Boulder Creek earthflow from 1964–1976. Deformation was determined automatically from two orthorectified aerial photos using COSI-Corr software. Vectors are indicative of relative magnitude and direction of movement and do not reflect true ground displacement.

Fig. 10. Map of gully density from a subset of the Eel River lidar data along the mainstem between Kekawaka Creek and Boulder Creek. Gully pixels (in black) are defined as having drainage areas of 3000 to 10^6 m^2 based on their distinctive morphologic signature, and gully density is the percent of these pixels in a moving window of radius 100 m. Areas of high gully density are commonly associated with active and recently active earthflows, outlined in white.

Fig. 11. Shaded relief map of Kekawaka Creek, tributary to the Eel River with in-situ cosmogenic radionuclide sampling sites superimposed. Inset image shows collection of megaboulders (>10 m diameter) that correspond with the upper end of the knickpoint zone. Profile of elevation and slope along Kekawaka Creek shows CRN sampling sites. Erosion rate values summarized in Table 1. The Lower Kekawaka erosion rate was calculated using the mixing model from Granger et al. (1996).

Fig. 12. InSAR velocity time series for 10 earthflows; twenty-day averaged precipitation shown in lower panel. Water years are outline with gray and white boxes. Precipitation data provided by NOAA rain gage located in Richardson Grove State Park near Garberville, CA. Db1 = Dobbyn Creek 1, Db2 = Dobbyn Creek 2, Lf = Lauffer Road, Kw1 = Kekawaka Creek 1, Kw2 = Kekawaka Creek 2, Kw3 = Kekawaka Creek 3, Cc = Chamise Creek, Bc = Boulder Creek, Lr = Lundblade Ranch, Sy = Simmerly Road. Modified from Handwerger et al. (2013).

Fig. 13. Analysis of suspended sediment data. A) Sediment rating curve (discharge, Q_w, vs. sediment concentration, C_s) for the Scotia, CA (Eel River) gauging station, for 1960-1963 and 1970-1980. Data for summer low flow conditions (Q_w < 35 m^3/s) were culled (see text).

LOWESS fit represents a moving average to the data. B) Variation of residuals from fit in A with water day for 14-yr dataset. Average daily precipitation is shown for the same period. Note that the progressive decline in residual values (which reflects hysteresis) experiences a positive excursion consistent with the timing of earthflow acceleration shown in Fig. 12.

Fig. 14. Histograms of average slope angles (in percent) for resistant blocks mapped in Fig. 4, active earthflows mapped in Fig. 7, and terrain underlain by argillaceous bedrock and inactive earthflows. Note that inactive and active earthflow terrain has indistinguishable slope distributions while resistant blocks have a much higher proportion of steep angles.

Table 1. Summary data for in-situ cosmogenic radionuclide analysis of stream sediments

Sample	Lat/Long	Grain Size (mm)	^{10}Be Concentration (atoms g^{-1})	Be AMS standardization	Watershed mean latitude	Watershed mean elevation (m)	Watershed effective elevation (m)	Watershed apparent basin-scale erosion rate (m Myr^{-1})	Watershed area (km^2)
KWCK-Input (above knickpoint)	40.094, -123.516	0.25-0.5	3.354E+04	KNSTD	40.0728	889	896	292.02 ± 16.91	51.6
KWCK-Mouth (Eel confluence)	40.115, -123.458	0.25-0.5	1.950E+04	KNSTD	40.0891	808	822	477.80 ± 29.17	85

Erosion rates were calculated following the production rate calibration data in Balco et al. (2008). Note that erosion rates for the upper and lower portions of the catchment were calculated using the mixing model employed by Granger et al. (1996).
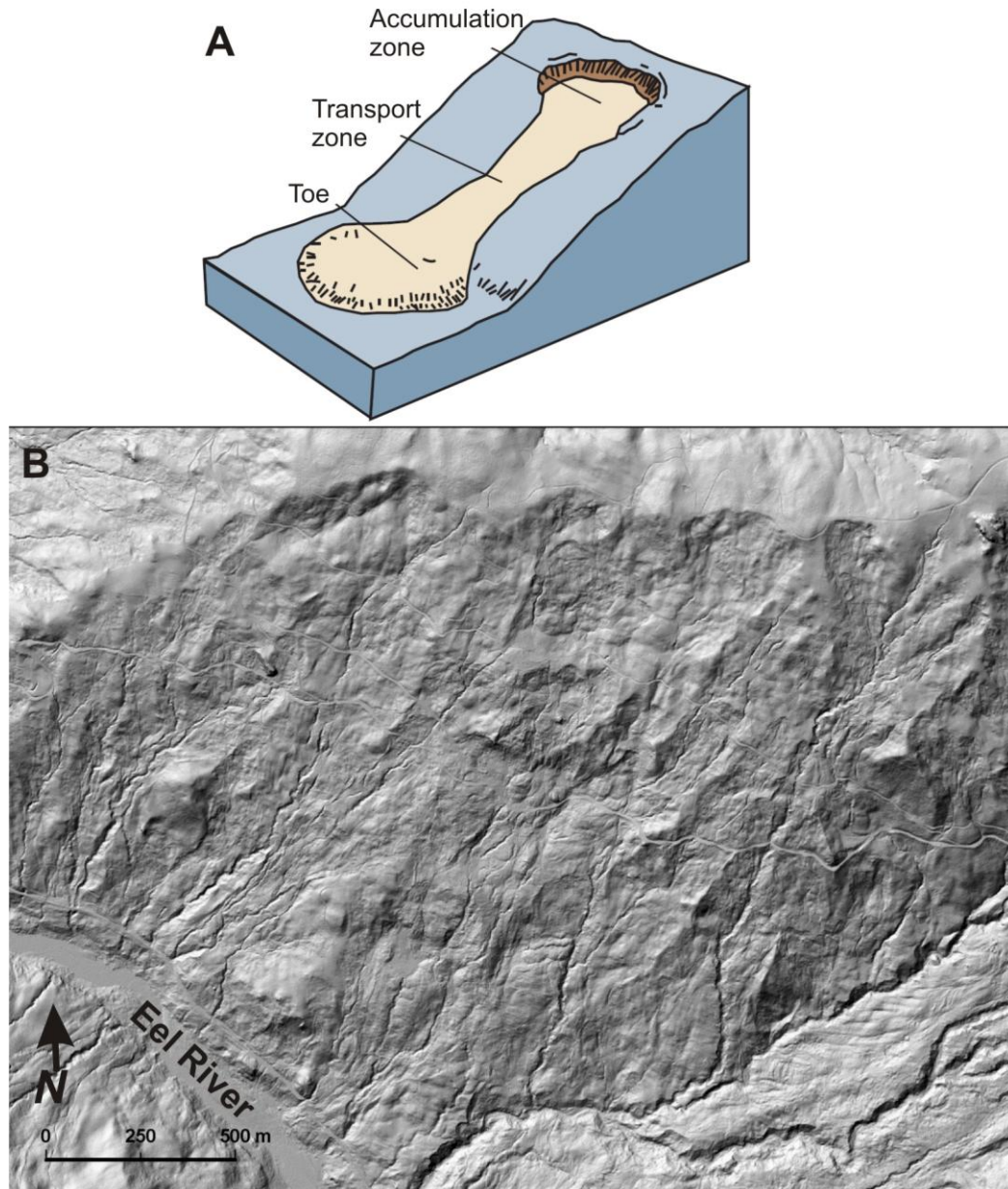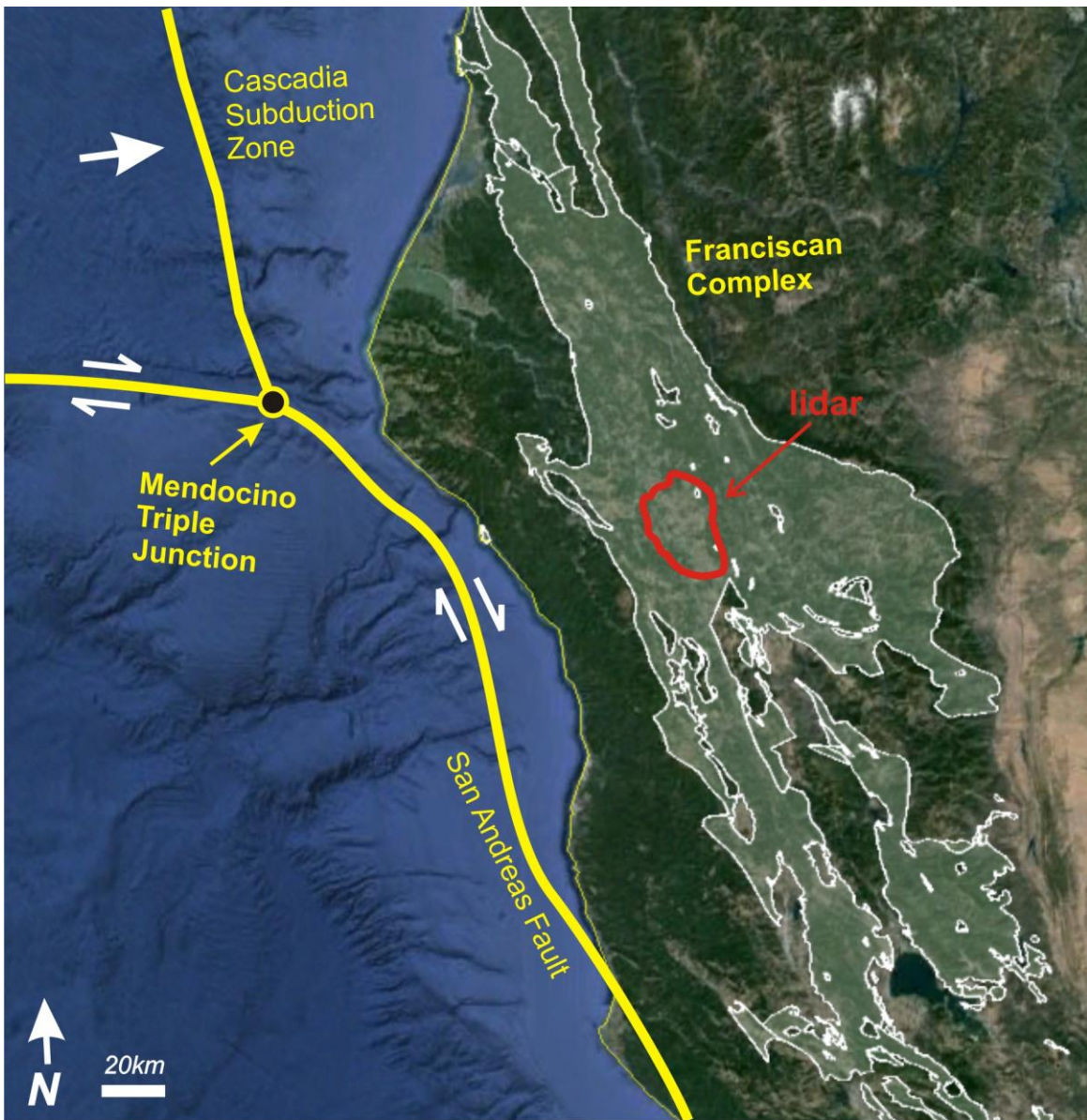
Fig. 1

Fig. 2
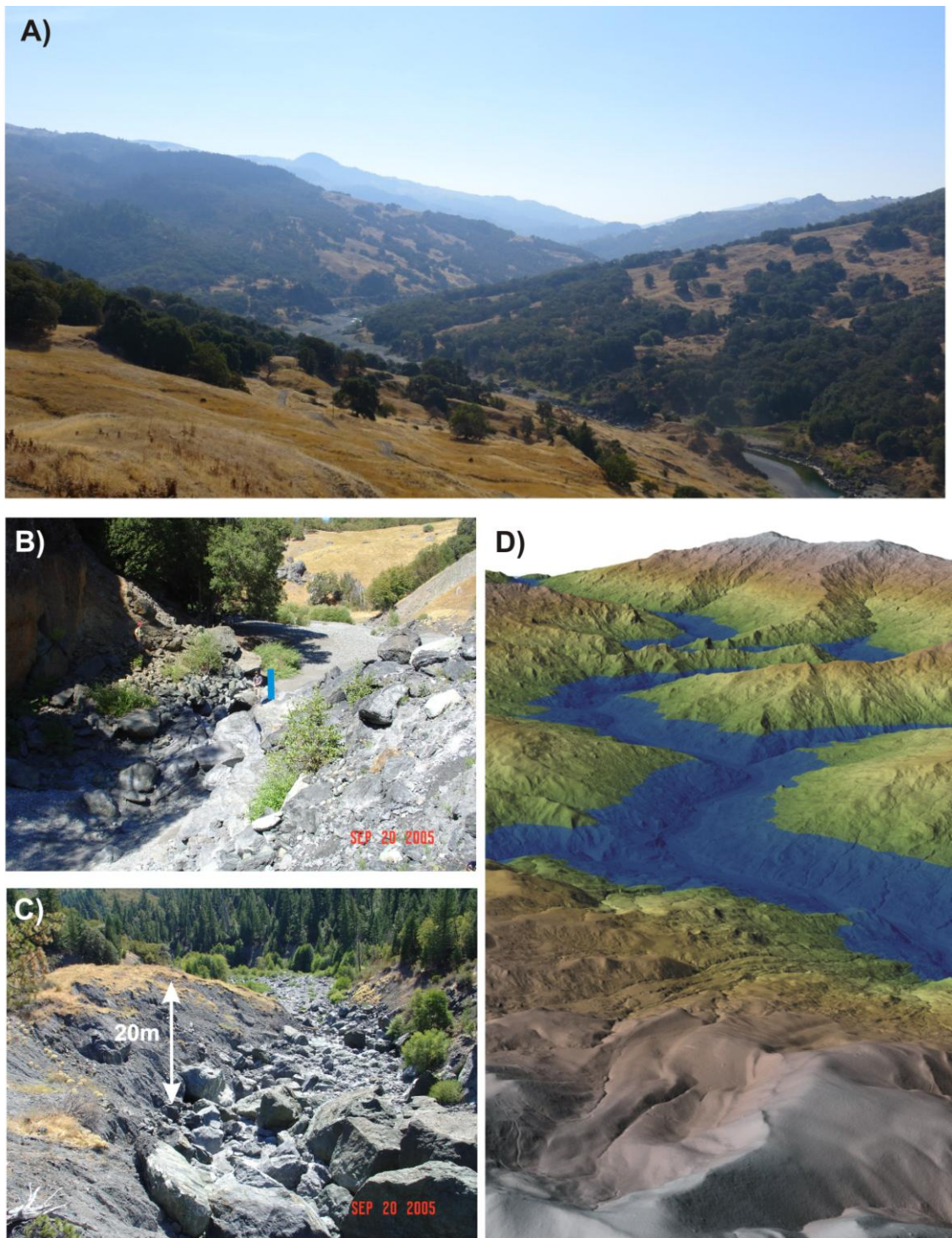
Fig. 3
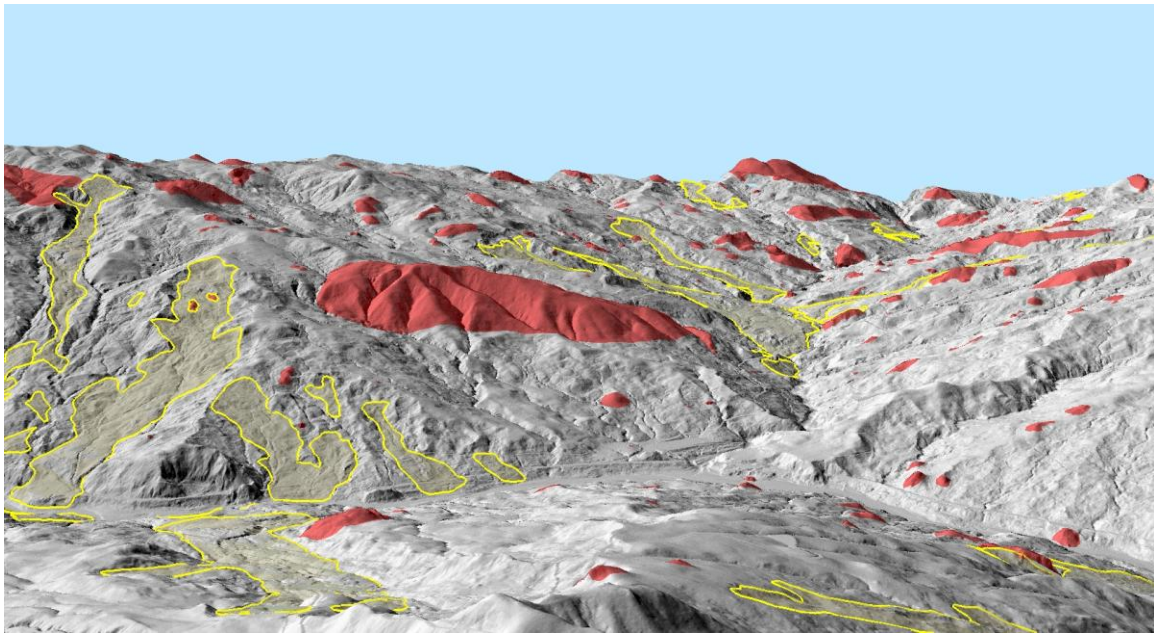
Fig. 4
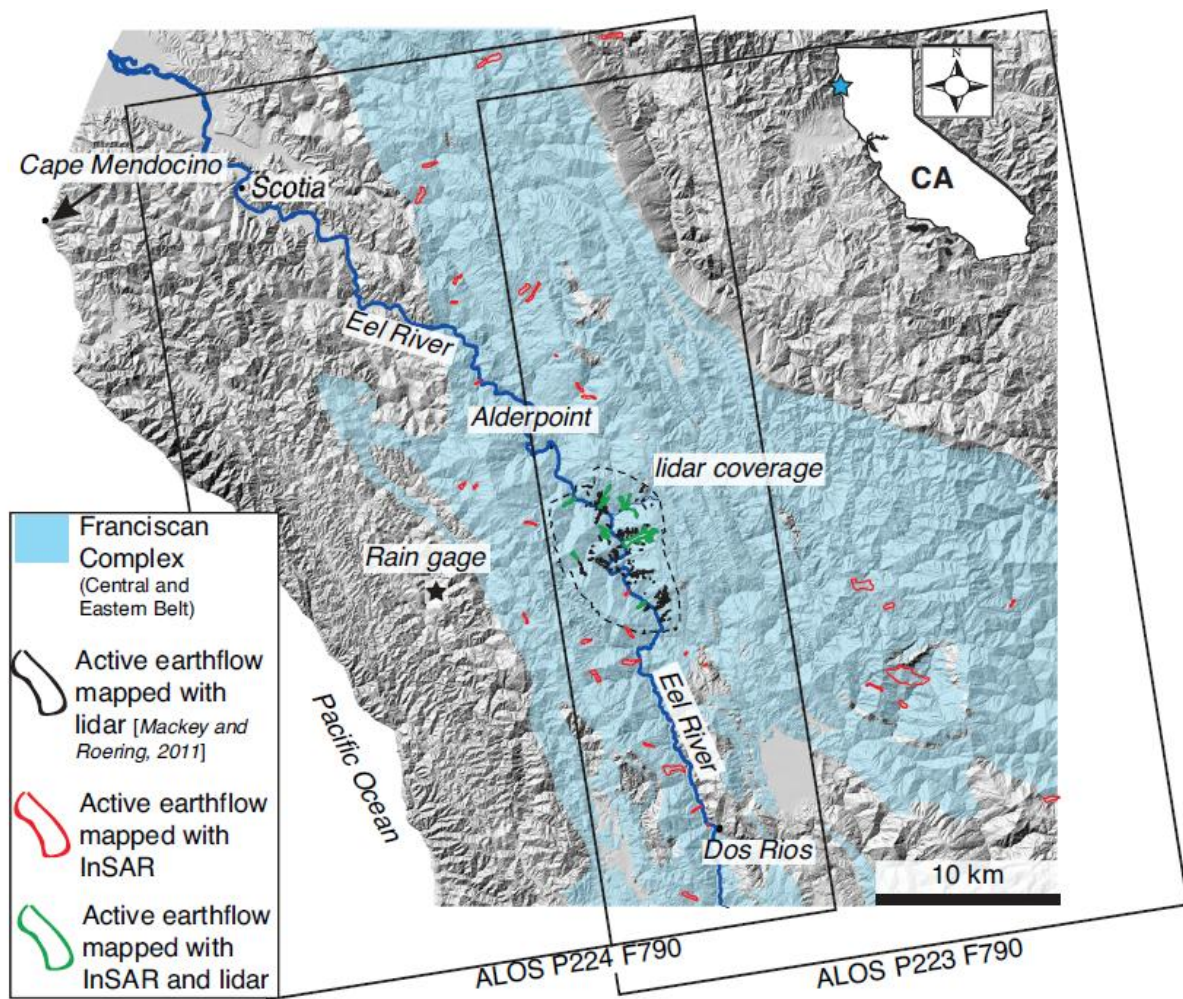
Fig. 5
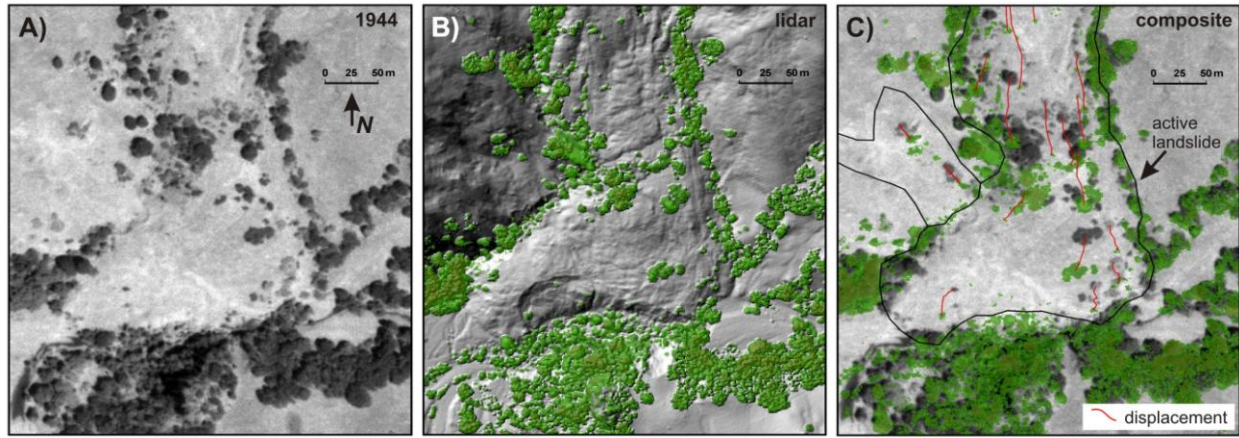
Fig. 6
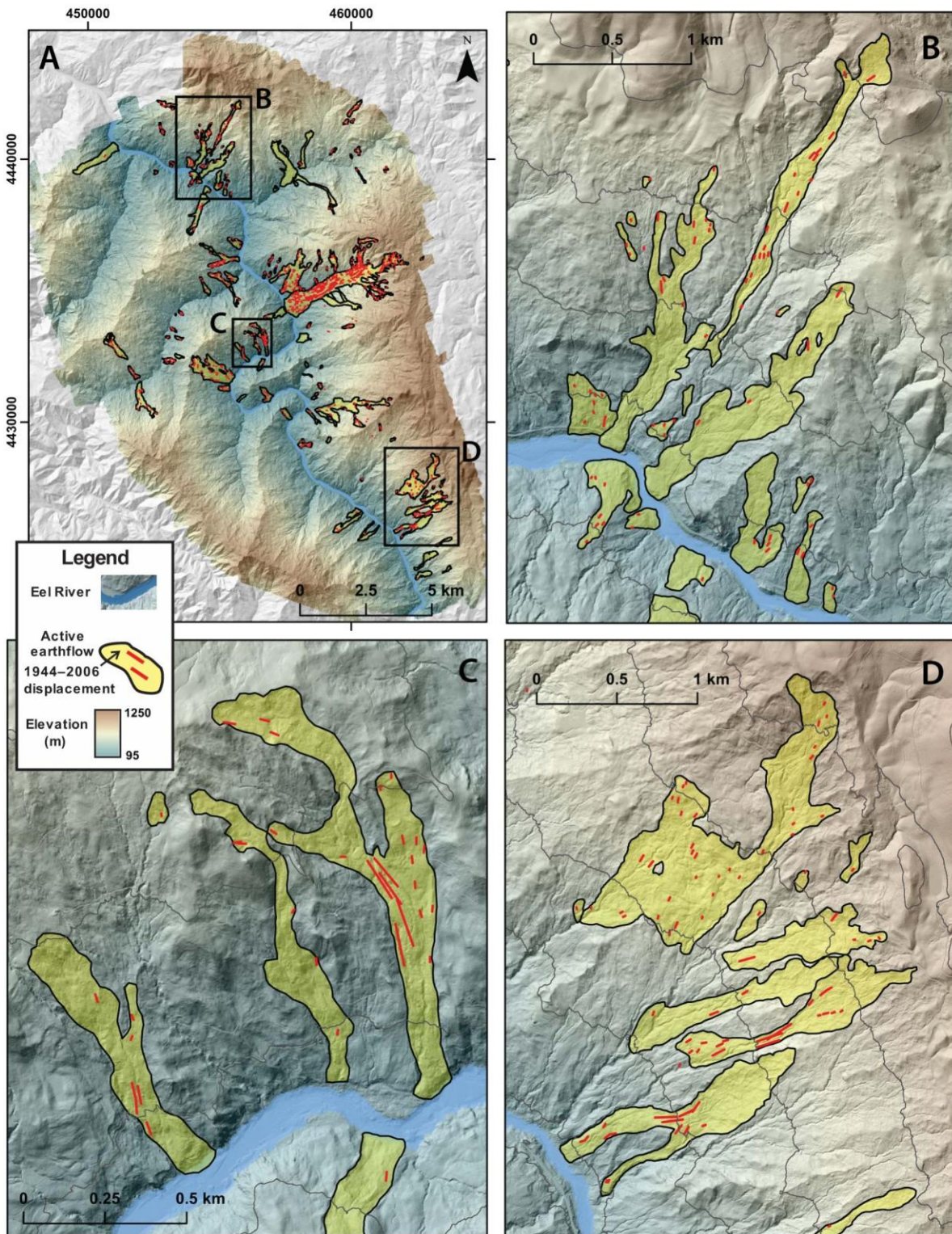
Fig. 7
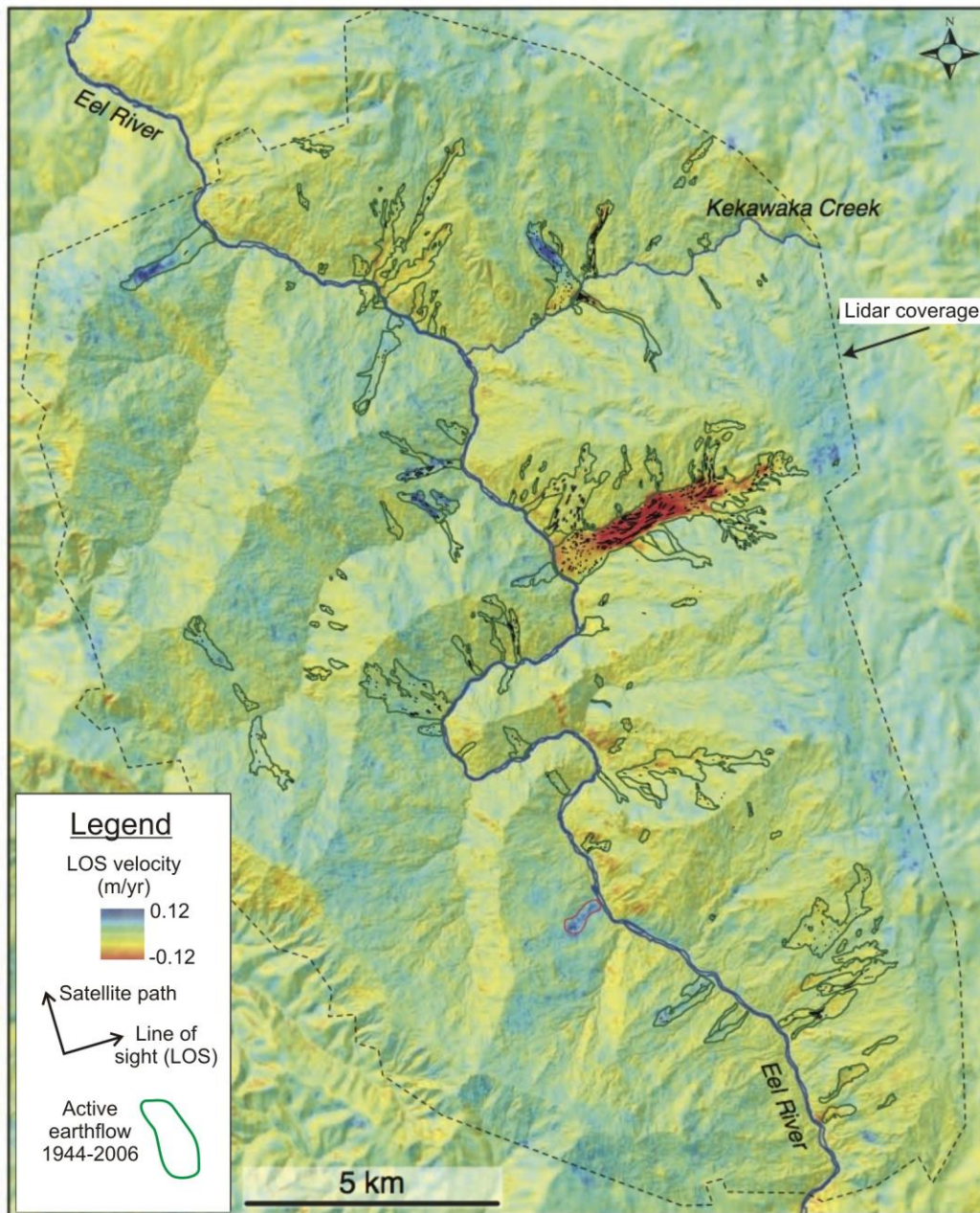
Fig. 8
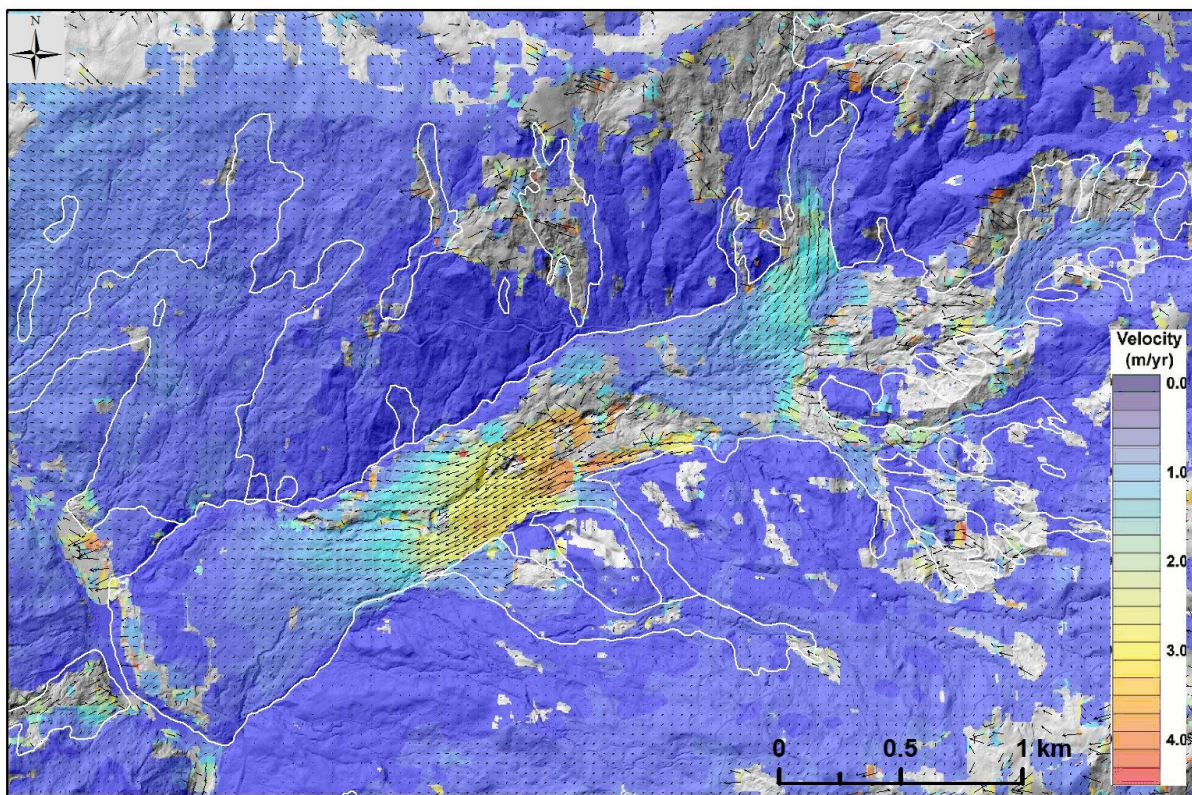
Fig. 9
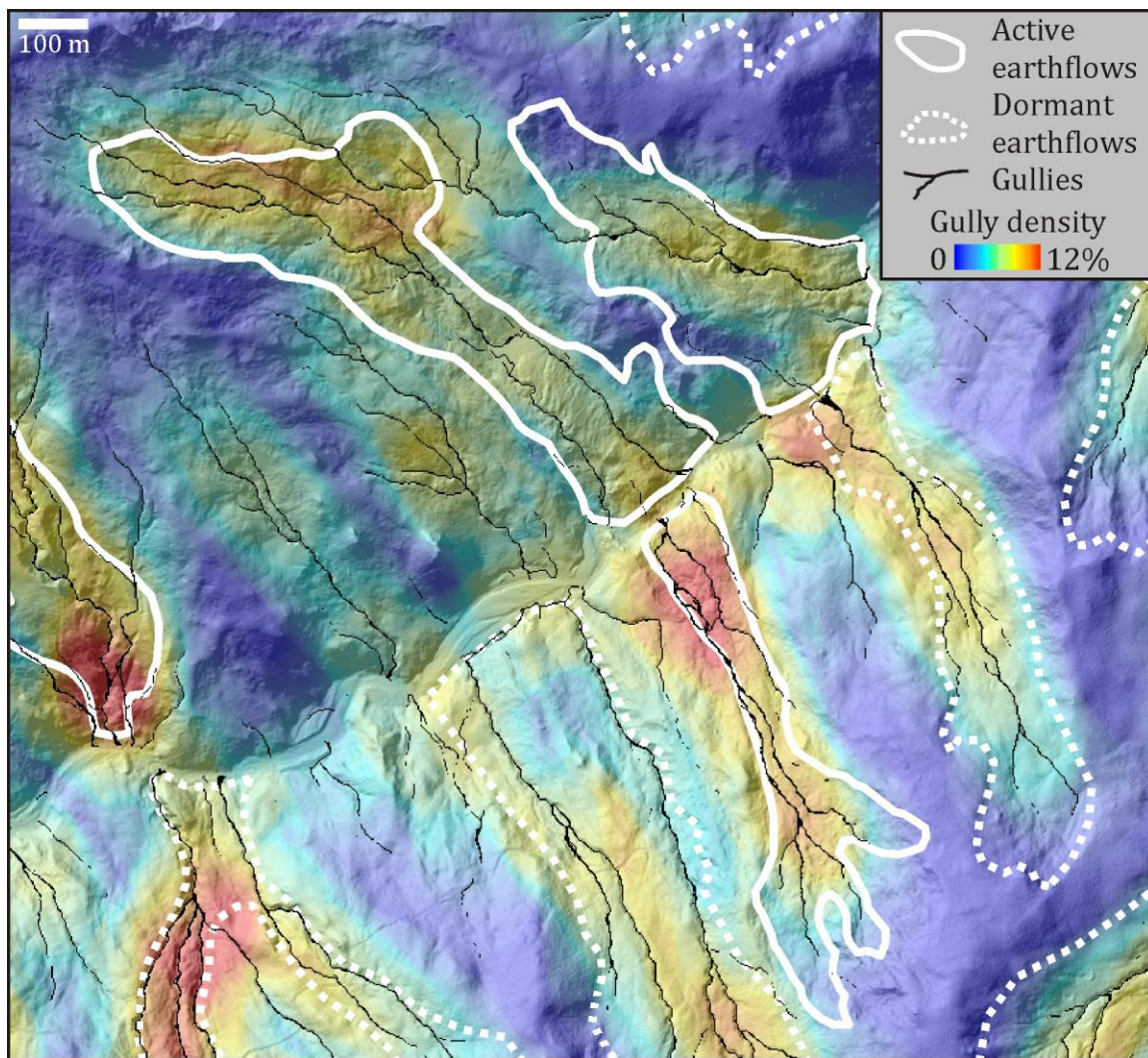
Fig. 10

Lower Kekewaka Crk
Avg. slope = 30%
Erosion = 0.76 mm/yr
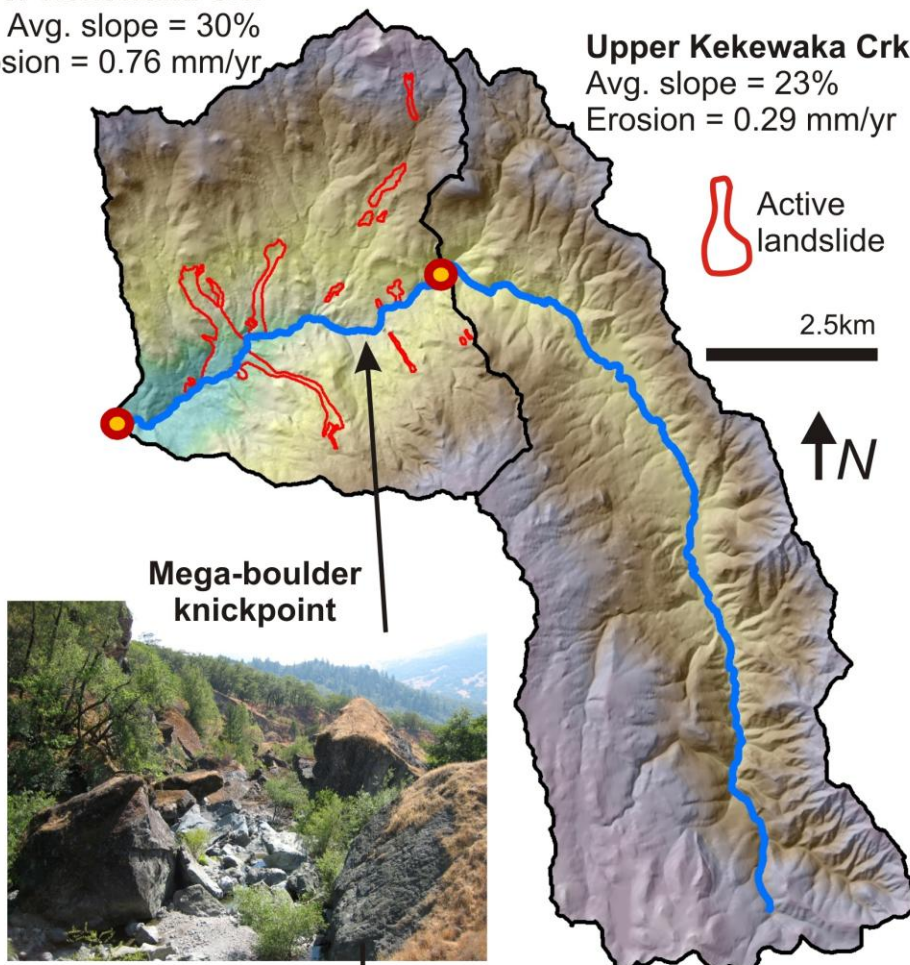
Upper Kekewaka Crk
Avg. slope = 23%
Erosion = 0.29 mm/yr

Active landslide

2.5km

N

**Mega-boulder knickpoint**

CRN sample locations
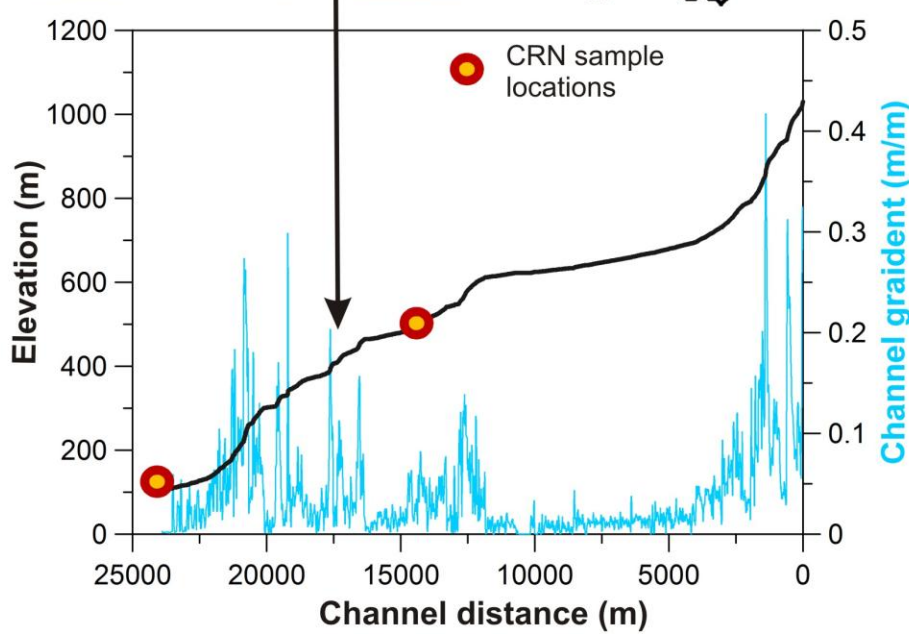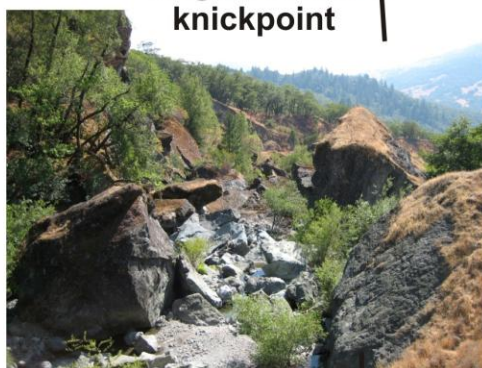
Fig. 11
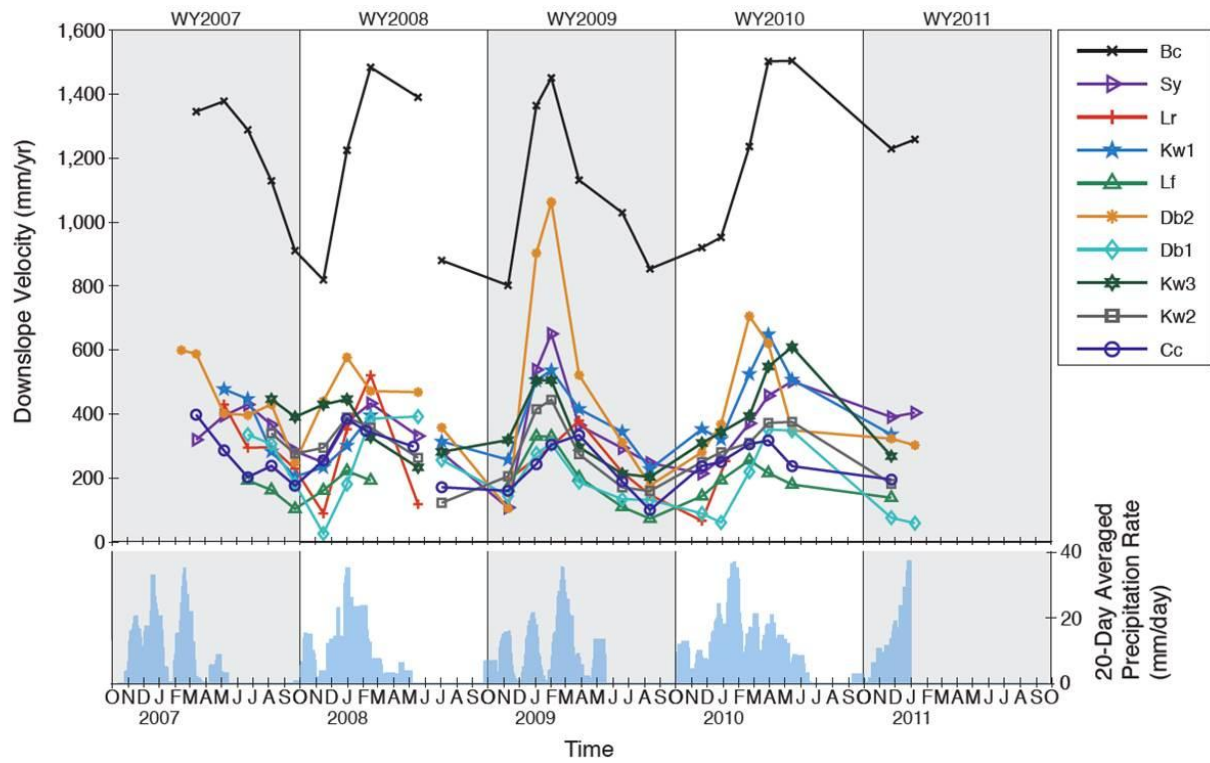
Fig. 12
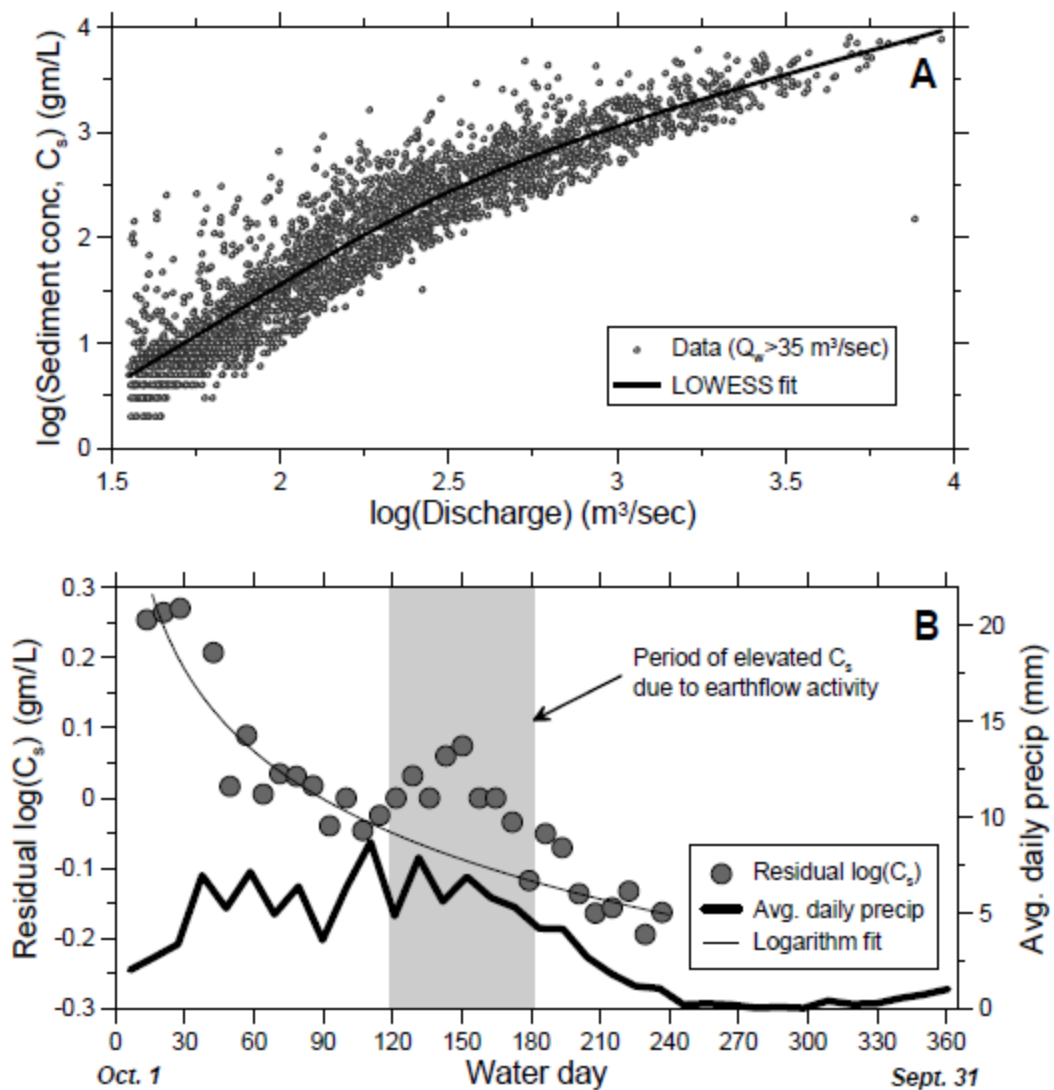
Fig. 13
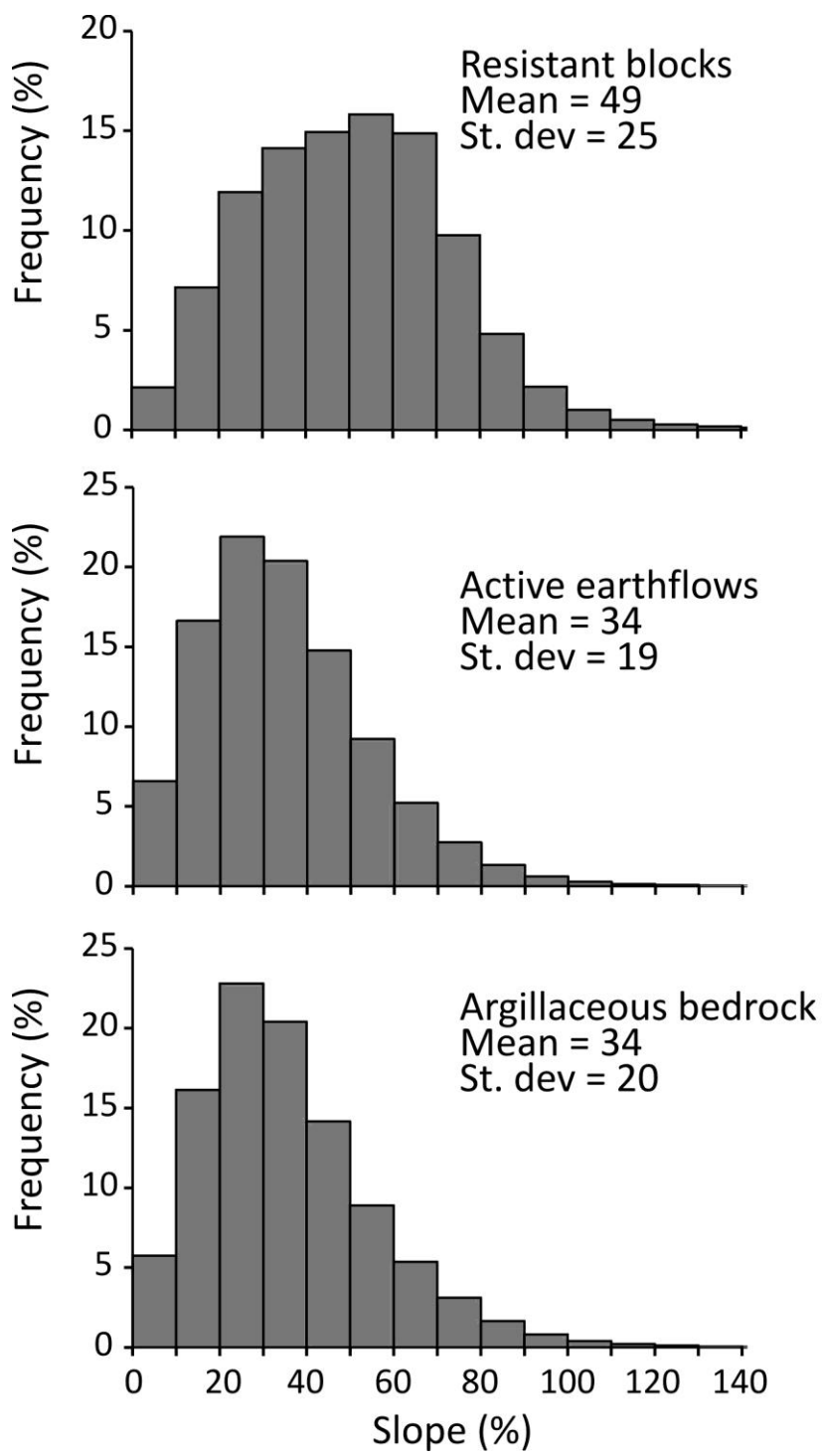
Fig. 14

Highlights

· We review diverse methods for exploring how landslides influence landscapes in rapidly uplifting regions of Northern California

· We use field data to explore and test the threshold slope concept and state-of-the-art landslide process models

· We analyze suspended sediment and cosmogenic nuclide erosion rates as well as seasonal landslide dynamics to determine the timescales over which landslide erosion balances rock uplift